Upwind stabilization of Navier-Stokes solvers

François Beux, Stephane Lanteri, Alain Dervieux, Bernard Larrouturou

UPWIND STABILIZATION OF NAVIER-STOKES SOLVERS

François BEUX
Stéphane LANTERI
Alain DERVIEUX
Bernard LARROUTUROU

Mars 1993

UPWIND STABILIZATION OF NAVIER-STOKES SOLVERS

STABILISATION DE SOLVEURS

NAVIER-STOKES PAR DECENTRAGE

François BEUX (*)

Stéphane LANTERI (*)

Alain DERVIEUX (*)

Bernard LARROUTUROU (**)

(*) INRIA Sophia-Antipolis
2004, route des Lucioles
06560 VALBONNE (FRANCE)
(**) CERMICS, INRIA Sophia-Antipolis
2004, route des Lucioles
06560 VALBONNE (FRANCE)

ABSTRACT :

We present a study of the effect of upwinding on stabilisation of both advective and pressure terms in a family of primitive-variable Navier-Stokes solvers. We consider two MUSCL Schemes, the first one applies to compressible flow, the second one to incompressible flow. We illustrate the fact that both numerical models suffer oscillations if a minimal (but not large) amount of upwinding is not associated with acoustics, while advection can be stabilized by the physical diffusion terms when the mesh Reynolds number is small enough.

RESUME :

On présente une étude de l'effet du décentrage sur la stabilisation des termes advectifs et de pression d'une famille de solveurs de Navier Stokes en variables primitives. On considère deux schémas MUSCL, l'un s'appliquant à des écoulements compressibles, l'autre à des écoulements incompressibles. On illustre le fait que les deux schémas présentent des oscillations si une quantité minimale de décentrage n'est pas appliquée aux termes "acoustiques", alors que les termes convectifs sont stabilisés pour des faibles Reynolds de maille par la diffusion physique du modèle.

Table des matières

INTRODUCTION

The stabilization of pressure terms in primitive-variables CFD methods is a very old problem. Clearly, schemes resulting in central-differenced three-point pressure first derivatives are not spatially stable.

One first way to overcome this difficulty has been to use **staggered grids** to emulate the stable two-point second-order Box differentiation, as in the MAC method [33].

Later on, the powerful theory of **mixed finite-element** (see e.g. [14]) allowed the design of stable discretisations over arbitrary meshes. Mixed finite element method like the Hood-Taylor $P_2 P_1$ approximation (see e.g. [29]) are now very popular and used for many industrial applications.

More recently, some interest has regained for non-staggered grids or non mixed finite elements: three families of such "**collocated**" schemes are studied.

In finite-element studies, the **mini-element** was introduced (see for example [11]); this mixed formulation can be reduced to a non-mixed one by eliminating the "extra" degree of freedom; in [21], it is shown that this introduces some numerical viscosity in the continuity equation; which may degrade the global accuracy. In the "**Least Square Galerkin methods**" [16], it is proposed that this diffusion term be a discretisation of one of the equations of the system, to be thus small for fine meshes, avoiding the degradation of accuracy.

Also a set of collocated methods has been generated from **fictive staggering**; we refer here to [23].

The third series of non-staggered investigations relies on **upwind schemes** applied to some extension of the artificial compressibility approach. We refer to [6] for some recent work in this direction. Upwind TVD schemes, like van Leer's and Osher's can then be adapted ; first-order versions yield matrices that are essentially diagonally dominant and that efficiently precondition second-order upwind approximations, as indicated by theoretical studies [4].

In this work, we are interested by upwind schemes and we present a set of experiments that tend to determine to which extent the different components of the artificial viscosity involved in the upwind formulation are necessary for spatial stability and accuracy.

In particular, we identify an advective component and an acoustic one in the numerical viscosity; we show that the advective part is not strictly necessary, but can be suppressed at low Reynolds numbers, and, in general, can be monitored by the mesh Reynolds number, as in mixed FEM formulations (see e.g. [1]).

We show that the acoustic numerical viscosity is necessary, especially in steady calculations; but it can be strongly reduced in many cases, which may result in a better accuracy.

This numerical study is performed for both incompressible and compressible models.

1   UPWIND SCHEMES FOR COMPRESSIBLE FLOWS

We are concerned here with the numerical simulation of two-dimensional viscous compressible flows that are modeled by the full Navier-Stokes equations. We first consider a simplified scalar model for advection-diffusion problems and introduce a family of three-parameters schemes based on an upwind discretization of the convective flux term and a classical centered approximation for the diffusive one. We next describe the two-dimensional extension of these schemes on unstructured triangular grids with the use of a mixed finite volume/finite element method for the spatial approximation of the convective and diffusive fluxes. Finally, results from unsteady and steady simulations around a NACA0012 airfoil are presented.

1.1   One-dimensional analysis

A simplified model that can be used to describe viscous flows is given by the linear advection-diffusion equation :

$$u_t + f(u)_x = \mu u_{xx} \ , \tag{1}$$

with $f(u) = cu$, where we assume $c > 0$ and $\mu > 0$. In the present study, numerical solutions of this equation are obtained via a family of three-parameters schemes characterized as follows:

- the convective flux term is discretized using a finite volume formulation where the numerical flux function is of the upwind type, while a linear interpolation method yields the left and right control volume boundary states;

- the diffusive flux term is computed using a classical three-points centered scheme;

- the temporal term approximation combines a mass-lumped and a consistent mass matrix formulation.

1.1.1   Spatial approximation

Let x_i , $i \in [0, N]$ denote the discretization points of the real interval $[0, 1]$ and Δx the constant mesh size. For each discretization point we state $u_i \approx u(x_i)$ and we define the control volume C_i as the interval $[x_{i-\frac{1}{2}}, x_{i+\frac{1}{2}}]$ where $x_{i+\frac{1}{2}} = \dfrac{x_i + x_{i+1}}{2}$. The advection-diffusion equation (1) is first discretized in space. For each discretization point x_i we obtain the following ordinary differential equation :

$$
\begin{aligned}
(1-\alpha)\frac{du_i}{dt} \quad &+\alpha \sum_{j \in \{i-1,i,i+1\}} \frac{du_i}{dt} \iint_{\Omega_h} N_i N_j d\omega \\
&+ \sum_{j \in \{i-1,i+1\}} \Phi^\delta(u_{ij}^\beta, u_{ij}^\beta) = v(u)_i
\end{aligned}
\tag{2}
$$

where the N_i are P1 canonical basis functions and :

$$v(u)_i \quad = \frac{\mu}{\Delta x^2}(u_{i-1} - 2u_i + u_{i+1}) \ . \tag{3}$$

In (3), Φ^δ is a numerical flux function of the upwind type, where the amount of artificial diffusion is weighted according to the value of the parameter δ :

$$\Phi^\delta(u_l, u_r) \quad = \frac{1}{2}[f(u_l) + f(u_r)] - \frac{\delta}{2}d(u_l, u_r) \ ,$$

$$d(u_l, u_r) \quad = \mid f'\left(\frac{u_l + u_r}{2}\right) \mid (u_r - u_l) \ . \tag{4}$$

In the linear case where $f(u) = cu$ the numerical flux function above reduces to :

$$\Phi^\delta(u_l, u_r) \quad = \frac{c}{2}[(1 + \delta)u_l + (1 - \delta)u_r] \ . \tag{5}$$

The left and right control volume boundary states u_l and u_r that are involved in equation (2) are computed using piecewise linear interpolation formulas :

$$u^\beta_{i,i+1} \quad = u_i \quad +(1 - \beta)\frac{u_{i+1} - u_i}{2} + \beta\frac{u_i - u_{i-1}}{2} \ ,$$

$$u^\beta_{i+1,i} \quad = u_{i+1} \quad -(1 - \beta)\frac{u_{i+1} - u_i}{2} - \beta\frac{u_{i+2} - u_{i+1}}{2} \ ,$$

$$u^\beta_{i,i-1} \quad = u_i \quad -(1 - \beta)\frac{u_i - u_{i-1}}{2} - \beta\frac{u_{i+1} - u_i}{2} \ ,$$

$$u^\beta_{i-1,i} \quad = u_{i-1} \quad +(1 - \beta)\frac{u_i - u_{i-1}}{2} + \beta\frac{u_{i-1} - u_{i-2}}{2} \ . \tag{6}$$

In the above expressions, β appears as an upwinding parameter that controls the combination of fully upwind and centered slopes. It is easy to verify that porting these expressions in the discretized equation (2) yields a five-point scheme. We denote:

$$g(u)_i = \sum_{j \in \{i-1, i+1\}} \Phi^\delta(u^\beta_{ij}, u^\beta_{ij}) = \quad \frac{c}{4\Delta x}((1 + \delta)\beta u_{i-2} - 2(1 + \beta + 2\delta\beta)u_{i-1}$$

$$+6\delta\beta u_i + 2(1 + \beta - 2\delta\beta)u_{i+1} \tag{7}$$

$$-(1 - \delta)\beta u_{i+2} \ .$$

The accuracy of these spatial approximations can be assessed using Taylor expansions. Applying this technique to $v(u)_i$ and $g(u)_i$ results in the following expression:

$$-g(u)_i + v(u)_i \quad = -cu_x + \mu u_{xx} \quad +c(3\beta - 1)\frac{\Delta x^2}{6}u_{xxx}$$

$$+ \left(\frac{\mu}{3} - \delta\beta c\Delta x\right)\frac{\Delta x^2}{4}u_{xxxx} + O(\Delta x^4) \ . \tag{8}$$

1.1.2   Temporal approximation

Looking at equation (2), we see that the temporal part combines a mass lumped term and a consistent mass matrix term. This yields a modified mass matrix formulation characterized by the matrix P_α defined by :

$$P_\alpha = (1 - \alpha)D + \alpha M \tag{9}$$

where D is the lumped diagonal mass matrix, viz. the identity matrix in this simplified case, and M is the consistant mass matrix associated with the P1 linear Lagrange element:

$$(MU)_j = \frac{u_{j-1} + 4u_j + u_{j+1}}{6} \ , \ \ U = u_j \tag{10}$$

Equation (2) can be now written in a matrix form :

$$P_\alpha U_t - \psi(U) = 0 \tag{11}$$

with :

$$\psi(U)_j = -g(u)_j + v(u)_j \tag{12}$$

Time integration is performed using a three–stage low–storage Runge-Kutta scheme:

$$\begin{cases} U^{(0)} = U^n = U(n\Delta t) \\[2mm] \begin{cases} MF(U^{(k)}) \ = \psi(U^{(k)}) \\[2mm] U^{(k)} \qquad = U^{(0)} + \dfrac{\Delta t}{1-k} F(U^{(k-1)}) \end{cases} \quad k = 1,2,3 \\[2mm] U^{(3)} = U^{(0)} + \Delta t F(U^{(3)}) = U^{n+1} \end{cases} \tag{13}$$

which involves the solution of a linear system; this can be achieved via a Jacobi iterative process.

1.1.3   Choosing the parameters

The accuracy of the complete approximation can be assessed using the Modified Equation Method (see [32]). For this purpose we use the previous expansion (8) on the spatial approximation. The modified equation of the scheme (1) up to the fourth order has the following form :

$$u_t + cu_x - \mu u_{xx} = D_3\left(\beta, \alpha\right)\frac{\Delta x^2}{6}u_{xxx} + D_4\left(\sigma, \beta, \alpha, \delta, Re_{\Delta x}\right)\frac{\Delta x^3}{6}u_{xxxx} + O(\Delta x^4) \tag{14}$$

where :

- D_3 is the coefficient of the dispersive derivative term u_{xxx} :

$$D_3 \left(\beta, \alpha \right) = c \left(3\beta - 1 + \alpha \right) \tag{15}$$

- D_4 is the coefficient of the dissipative derivative term u_{xxxx} :

$$D_4 \left(\sigma, \beta, \alpha, \delta, Re_{\Delta x} \right) = \frac{c}{2} \left(-3\beta\delta - \frac{(2\alpha - 1)}{Re_{\Delta x}} - \frac{\sigma^3}{2} \right) \tag{16}$$

Here, $\sigma = \dfrac{c\Delta t}{\Delta x}$ is the Courant number and $Re_{\Delta x} = \dfrac{c\Delta x}{\mu}$ is the mesh Reynolds number.

We shall now exhibit a number of optimal numerical schemes characterized by particular values given to the three parameters α , β and δ . In doing this, we would like to reach the following goals :

- for unsteady simulations, it is of particular interest to minimize the dispersive error; in the following we shall exhibit numerical schemes with zero linear dispersive error $(D_3 = 0)$;

- as we are interested in viscous flow simulations, we should minimize the dissipative error of the numerical scheme, that is, minimize the coefficient D_4 .

The following schemes can be considered as optimal according to the previous goals :

- $\alpha = 0$, $\delta = 1$ and $\beta = \dfrac{1}{3}$: third-order biased upwind scheme for the advection equation (see Desideri, Selmin and Goudjo [3]);

- $\alpha = 0$, $\delta = 0$ and $\beta = \dfrac{1}{3}$: third-order biased five–point centered scheme;

- $\alpha = 1$, $\delta = 0$ and $\beta = 0$: consistent mass-matrix three-point centered scheme, with the classical Galerkin approximation for the advection equation (which is fourth-order accurate in space on uniform grids);

- $\alpha = \dfrac{1}{2}$, $\delta = 0$ or 1 and $\beta = \dfrac{1}{6}$: modified mass-matrix scheme, Galerkin-like approximation for the advection-diffusion equation (which is fourth-order accurate in space on uniform grids).

When $\alpha = 0$ and for any δ, the linear dispersive error term of (14) in equal to zero when $\beta = \dfrac{1}{3}$; in this case we shall minimize the dissipative error by using small values of the parameter δ . Nevertheless, the corresponding numerical scheme may lack of dissipation and spurious oscillations may appear in the convection-dominated parts of the flow (the extreme case being obtained when $\delta = 0$).

1.2 Two-dimensional extension

We now consider the extension of the previous schemes to the two-dimensional Navier-Stokes equations.

First we recall the mathematical problem to be solved and set some definitions and notations which are used in the sequel.

1.2.1 Governing equations

Let $\Omega \subset I\!\!R^2$ be the flow domain of interest and Γ be its boundary. The conservative law form of the equations describing two-dimensional compressible viscous flows is given by:

$$\frac{\partial W}{\partial t} + \vec{\nabla}.\vec{\mathcal{F}}(W) = \frac{1}{Re}\vec{\nabla}.\vec{\mathcal{R}}(W) \qquad (17)$$

where

$$W = (\rho \ , \ \rho u \ , \ \rho v \ , \ E)^T \quad , \quad \vec{\nabla} = \left(\frac{\partial}{\partial x} \ , \ \frac{\partial}{\partial y}\right)^T$$

$$\vec{\mathcal{F}}(W) = \begin{pmatrix} F(W) \\ G(W) \end{pmatrix} \quad , \quad \vec{\mathcal{R}}(W) = \begin{pmatrix} R(W) \\ S(W) \end{pmatrix}$$

The functions $F(W)$ and $G(W)$ denote the so-called "convective" or "Euler" fluxes written as :

$$F(W) = \begin{pmatrix} \rho u \\ \rho u^2 + p \\ \rho uv \\ u(E + p) \end{pmatrix} \quad , \quad G(W) = \begin{pmatrix} \rho v \\ \rho uv \\ \rho v^2 + p \\ v(E + p) \end{pmatrix}$$

while the functions $R(W)$ and $S(W)$ are the diffusive fluxes :

$$R(W) = \begin{pmatrix} 0 \\ \tau_{xx} \\ \tau_{xy} \\ u\tau_{xx} + v\tau_{xy} + \frac{\gamma k}{Pr}\frac{\partial \varepsilon}{\partial x} \end{pmatrix} \quad , \quad S(W) = \begin{pmatrix} 0 \\ \tau_{xy} \\ \tau_{yy} \\ u\tau_{xy} + v\tau_{yy} + \frac{\gamma k}{Pr}\frac{\partial \varepsilon}{\partial y} \end{pmatrix}$$

where ρ is the density, $\vec{U} = (u, v)$ is the velocity vector, E is the total energy per unit of volume; p is the pressure of the fluid, with the equation of state given for a perfect gas as :

$$p = (\gamma - 1)(E - \frac{1}{2}\rho \parallel \vec{U} \parallel^2)$$

γ is the ratio of specific heats ($\gamma = 1.4$ for air); ε denotes the specific internal energy related to the temperature by :

$$\varepsilon = C_v T = \frac{E}{\rho} - \frac{1}{2}(\parallel \vec{U} \parallel^2)$$

In the expressions for the diffusive fluxes, τ_{xx}, τ_{xy} and τ_{yy} are the Cauchy's stress tensor components given by :

$$\tau_{xx} = \frac{2}{3}\left(2\frac{\partial u}{\partial x} - \frac{\partial v}{\partial y}\right) \quad , \quad \tau_{yy} = \frac{2}{3}\left(2\frac{\partial v}{\partial y} - \frac{\partial u}{\partial x}\right) \quad , \quad \tau_{xy} = \left(\frac{\partial u}{\partial y} + \frac{\partial v}{\partial x}\right)$$

Lastly, Re and Pr are respectively the Reynolds and Prandtl numbers.

We are mostly interested in external flows around airfoils; then the domain of computation Ω is delimited by the boundary Γ, which we decompose as $\Gamma = \Gamma_b \cup \Gamma_\infty$. Let $\vec{n}$ be the outward unit normal at any point of the boundary Γ .

The flow is assumed to be uniform at the farfield boundary Γ_∞:

$$\rho_\infty = 1 \quad , \quad \vec{U}_\infty = \begin{pmatrix} cos\theta \\ sin\theta \end{pmatrix} \quad , \quad p_\infty = \frac{1}{\gamma M_\infty^2} \tag{18}$$

where θ is the angle of attack and M_∞ denotes the free-stream Mach number. On the wall boundary Γ_b, we assume the no-slip condition together with a Dirichlet condition on the temperature :

$$\vec{U} = 0 \quad , \quad T = T_b \tag{19}$$

while the density is free of any condition; the total energy per unit of volume and the pressure on the wall are then given by :

$$E = \rho C_v T_b \quad , \quad p = (\gamma - 1)E \tag{20}$$

1.2.2   Spatial discretization

The spatial discretization, which is referred to as MUSCL–FEM in previous papers [9, 25], is a standard Galerkin (continuous, piecewise linear) approximation for diffusion terms, and a finite volume one for hyperbolic terms, the finite volumes being designed in order to be compatible with the Galerkin method (see [5]).

We assume that Ω is a polygonal bounded domain of $I\!\!R^2$. Let $\mathcal{T}_h$ be a standard triangulation of Ω and h the maximal length of the edges of the triangles of $\mathcal{T}_h$. We need to introduce the following notations.

For every vertex $S_i (i = 1, ..., ns)$ of $\mathcal{T}_h$, the control volume C_i is the union of all those subtriangles resulting from the subdivision of each triangle by means of the medians who have S_i as a vertex (see Figure 1). The boundary of C_i is denoted by ∂C_i and the unit vector of the outward normal to ∂C_i by $\vec{\nu}_i = (\nu_{ix}, \nu_{iy})$. The union of all these control volumes constitutes a partition of domain Ω :
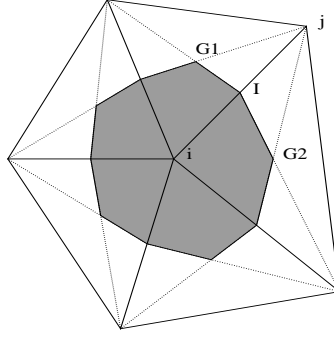
$$\Omega_h = \bigcup_{i=1}^{ns} C_i$$

Figure 1 : Control volume definition

For every vertex S_i, $K(i)$ is the set of neighboring nodes of S_i. We recall that Ψ_i is the characteristic function of the control volume C_i defined as :

$$\Psi_i(\vec{X}) = \begin{cases} 1 & \text{if} \quad \vec{X} \in C_i \\ 0 & \text{otherwise} \end{cases}$$

We introduce the following discrete spaces (where P_1 is the space of polynomials in two variables of degree 1) :

$$\mathcal{V}_h \;\; = \{v_h \mid v_h \in C^0(\Omega), v_h \mid_T \in P_1, \forall T \in \mathcal{T}_h\}$$

$$\mathcal{W}_h \;\; = \{v_h \mid v_h \in L^2(\Omega), v_h \mid_{C_i} = v_i = \text{const}; i = 1, ..., ns\}$$

In the finite element method, any function f belonging to $\mathcal{V}_h$ is uniquely determined by its values $f(S_i)$ at each vertex S_i and if we note $(N_i)_{i=1}^{ns}$ the basis set of $\mathcal{V}_h$, we have :

$$f(\vec{X}) = \sum_{i=1,ns} f(S_i) N_i(\vec{X})$$

There exists a natural bijection between spaces $\mathcal{V}_h$ and $\mathcal{W}_h$ defined by :

$$\forall f \in \mathcal{V}_h \;\; , \;\; S(f(\vec{X})) = \sum_{i=1,ns} f(S_i) \Psi_i(\vec{X})$$

First a general variational approach of equation (17) is derived :

$$\text{Find} \;\; W_h \in (\mathcal{V}_h)^4, \;\; \forall \varphi_h \in \mathcal{V}_h$$

$$\iint\limits_{\Omega_h} \frac{\partial W_h}{\partial t}\varphi_h dxdy \quad + \iint\limits_{\Omega_h} \vec{\nabla}.\vec{\mathcal{F}}(W_h)\varphi_h dxdy$$
$$= \frac{1}{Re}\iint\limits_{\Omega_h} \vec{\nabla}.\vec{\mathcal{R}}(W_h)\varphi_h dxdy \tag{21}$$

Then, a mixed finite volume/Galerkin finite element approximation is obtained by using different techniques for computing the left and right-hand-side integrals of (21). Let φ_h be the shape function N_i associated with the node S_i. We apply the operator S to the left-hand-side integral of (21) which results in the following formulation :

$$\iint\limits_{C_i} \frac{\partial W_h}{\partial t}dxdy \quad + \iint\limits_{C_i} \vec{\nabla}.\vec{\mathcal{F}}(W_h)dxdy$$
$$= \frac{1}{Re}\iint\limits_{SupN_i} \vec{\nabla}.\vec{\mathcal{R}}(W_h)N_i dxdy \tag{22}$$

where $SupN_i = \bigcup\limits_{T,S_i \in T} T$. In the next step, the convective term integral of (22) is treated using Green's formula while an integration by parts is applied on the diffusive one, which leads to :

$$\iint\limits_{C_i} \frac{\partial W_h}{\partial t}dxdy \quad + \int\limits_{\partial C_i} \vec{\mathcal{F}}(W_h).\vec{\nu}_i d\sigma$$
$$= -\frac{1}{Re}\sum\limits_{T,S_i \in T}\iint\limits_{T} \vec{\mathcal{R}}(W_h).\nabla \vec{N}_i^T dxdy \tag{23}$$
$$+\frac{1}{Re}\int\limits_{\Gamma_h} \vec{\mathcal{R}}(W_h).\vec{\nu}_i N_i d\sigma$$

where N_i^T is the restriction of N_i to triangle T. By neglecting the right-hand-side boundary integral of (23) (see the above remarks on boundary conditions), we obtain :

$$\iint\limits_{C_i} \frac{\partial W_h}{\partial t}dxdy \quad + \sum\limits_{j\in K(i)}\int\limits_{\partial C_{ij}} \vec{\mathcal{F}}(W_h).\vec{\nu}_{ij}d\sigma \qquad <1>$$
$$+ \int\limits_{\partial C_i \cap \Gamma_b} \vec{\mathcal{F}}(\bar{W}_h).\vec{n}_i d\sigma \qquad <2>$$
$$+ \int\limits_{\partial C_i \cap \Gamma_\infty} \vec{\mathcal{F}}(\bar{W}_h).\vec{n}_i d\sigma \qquad <3> \tag{24}$$
$$= -\frac{1}{Re}\sum\limits_{T,S_i \in T}\iint\limits_{T} \vec{\mathcal{R}}(W_h).\nabla \vec{N}_i^T dxdy \quad <4>$$

Specifying the approximation for computing the integrals in (24) completes the description of the spatial integration scheme.

In the above formulation, it is important to remark that the computation of the convective terms (that is the integral involving $\mathcal{F}$) is now performed in a one-dimensional manner : convective fluxes are computed along the normal direction $\vec{\nu}$. For this purpose, the boundary ∂C_i of the control volume C_i is split into bi-segments ∂C_{ij} which join the middle point of the segment $[ij]$ to the centroids of the triangle having S_i and S_j as common vertices (see Figure 2).
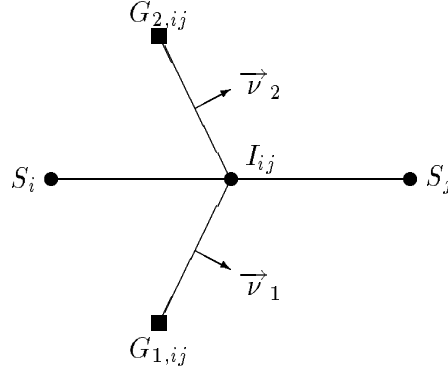

Figure 2 : Definition of ∂C_{ij}

The computation of the convective term $< 1 >$ in (24) is decomposed between the adjacent cells to cell C_i :

$$\sum_{j \in K(i)} \int_{\partial C_{ij}} \vec{\mathcal{F}}(W_h).\vec{\nu}_{ij} d\sigma = \sum_{j \in K(i)} \vec{\mathcal{F}}(\tilde{U}). \int_{\partial C_{ij}} \vec{\nu}_{ij} d\sigma \qquad (25)$$

where $\vec{\mathcal{F}}(\tilde{U})$ is some approximation of the convective flux computed at the interface between cells C_i and C_j. Upwinding is introduced in the computation of this term through the use of a numerical flux function Φ :

$$H_{ij}^{(1)} = \Phi^\delta_{\mathcal{F}_{ij}}(W_i, W_j, \vec{\nu}_{ij})$$

where $W_i = W_h(S_i)$ and $W_j = W_h(S_j)$. The numerical flux functions used in this study is a weighted diffusion version of the one proposed by Roe [24]:

$$\Phi^\delta_{\mathcal{F}}(U, V, \vec{\nu}) = \frac{\mathcal{F}(U, \vec{\nu}) + \mathcal{F}(V, \vec{\nu})}{2} - K^\delta d(U, V, \vec{\nu}) \qquad (26)$$

where $d(U, V, \vec{\nu})$ is the numerical diffusivity term which is defined by :

$$d\left(U,V,\vec{\nu}\right) = \mid A\left(\tilde{W},\vec{\nu}\right) \mid \frac{(V-U)}{2}, \quad |A| = T| \wedge |T^{-1}, \quad A = T \wedge T^{-1} \qquad (27)$$

$\tilde{W}$ is the Roe average of U et V [24], and $\wedge$ the diagonal matrix defined by :

$$
\begin{aligned}
\lambda_1 &= \lambda_1\left(\tilde{W},\vec{\nu}\right) &= \tilde{\vec{U}}.\vec{\nu} \\
\lambda_2 &= \lambda_2\left(\tilde{W},\vec{\nu}\right) &= \lambda_1\left(\tilde{W},\vec{\nu}\right) \\
\lambda_3 &= \lambda_3\left(\tilde{W},\vec{\nu}\right) &= \lambda_1\left(\tilde{W},\vec{\nu}\right) + \parallel\vec{\nu}\parallel \\
\lambda_4 &= \lambda_4\left(\tilde{W},\vec{\nu}\right) &= \lambda_1\left(\tilde{W},\vec{\nu}\right) - \parallel\vec{\nu}\parallel
\end{aligned}
\qquad (28)
$$

Moreover, K^δ is a matrix of weighting coefficients for the components of the diffusion term :

$$K^\delta = T \begin{pmatrix} \delta & 0 & 0 & 0 \\ 0 & \delta & 0 & 0 \\ 0 & 0 & \delta & 0 \\ 0 & 0 & 0 & \delta \end{pmatrix} T^{-1}. \qquad (29)$$

The last term $<4>$ of the right-hand side of (24) is computed using the classical $P1$ Galerkin finite element method resulting in a centered scheme. For this purpose, we first remark that the computation of the stress tensor components in the expressions for $R(W)$ and $S(W)$, result in constant values on each triangle are the values of the components of $\nabla\vec{N}_i^T$.

then the computation of term $<4>$ of (24) is simply stated as :

$$\sum_{T,S_i\in T} \iint_T \vec{\mathcal{R}}(W_h).\nabla\vec{N}_i^T dxdy = \sum_{T,S_i\in T} area(T)(R_T\frac{\partial N_i^T}{\partial x} + S_T\frac{\partial N_i^T}{\partial y}) \qquad (30)$$

where R_T and S_T are constant values of $R(W)$ and $S(W)$ on triangle T.

1.2.3   Acoustic damping

We define here a modified version of the numerical flux function of Roe [24] based on a the distinction of the advective and accoustic parts of the numerical diffusion.

$$\tilde{\Phi}^\delta_{\mathcal{F}}\left(U,V,\vec{\nu}\right) = \frac{\mathcal{F}(U,\vec{\nu}) + \mathcal{F}(V,\vec{\nu})}{2} - \tilde{K}^\delta d(U,V,\vec{\nu}) \qquad (31)$$

where, $\tilde{K}^\delta$ is the diagonal matrix :

$$\tilde{K}^\delta = T \begin{pmatrix} 0 & 0 & 0 & 0 \\ 0 & 0 & 0 & 0 \\ 0 & 0 & \delta & 0 \\ 0 & 0 & 0 & \delta \end{pmatrix} T^{-1}. \qquad (32)$$

1.2.4 Higher-order approximation

The numerical integration with an upwind scheme as described above leads to approximations which are only first-order accurate. We present a MUSCL (Monotonic Upwind Scheme for Conservation Laws [31]) extension of scheme (24) in order to get a second-order accurate solution.

Following the M.U.S.C.L. method, one way to reach the second-order spatial accuracy is to evaluate fluxes with extrapolated values W_{ij}, W_{ji} at the interface $\partial C_i \cap \partial C_j$. This leads to the following modification of the computation of the term $H_{ij}^{(1)}$:

$$H_{ij}^{(2)} = \Phi_{\mathcal{F}_{ij}}(W_{ij}, W_{ji}, \vec{\nu}_{ij})$$

$$W_{ij}^{\star} = W_i^{\star} + \frac{1}{2}(\vec{\nabla}W)_{ij}^{\star}.\vec{ij}$$

$$W_{ji}^{\star} = W_j^{\star} - \frac{1}{2}(\vec{\nabla}W)_{ji}^{\star}.\vec{ij}$$

(33)

where $W^{\star} = (\rho \ , \ u \ , \ v \ , \ p)^T$ and where the approximate nodal gradients $(\vec{\nabla}W)_{ij,ji}^{\star}$ are obtained using a β-combination of centered and fully upwind gradients :

$$(\vec{\nabla}W)_{ij}^{\star}.\vec{ij} = (\vec{\nabla}W)_{ij}^{\beta}.\vec{ij} = (1-\beta)(\vec{\nabla}W)_{ij}^{Cent}.\vec{ij} + \beta(\vec{\nabla}W)_{ij}^{Upw}.\vec{ij}$$

(34)

where the centered gradient $(\nabla\vec{W})_{ij}^{Cent}$ (obtained for $\beta = 0$), is any vector such that :

$$(\nabla\vec{W})_{ij}^{Cent}.\vec{ij} = W_j^{\star} - W_i^{\star}$$

(35)

The fully upwind gradient (obtained for $\beta = 1$) is computed according to the definition of the downstream and upstream triangles which can be associated with an edge $[S_i, S_j]$:

$$\begin{cases} (\vec{\nabla}W)_{ij}^{Upw} & = \vec{\nabla}W^G \mid_{T_{ij}} \\ (\vec{\nabla}W)_{S_j S_i}^{Upw} & = \vec{\nabla}W^G \mid_{T_{ji}} \end{cases}$$

(36)

where $\vec{\nabla}W^G \mid_T = \sum_{k \in T} W_k^{\star}\vec{\nabla}N_k^T$ is the P1 Galerkin gradient on triangle T and where T_{ij} and T_{ji} are defined as shown on Figure 3.

Notice that no slope limitation is used here before we use the interpolated values for the evaluation of the second-order accurate fluxes.

1.2.5 Boundary conditions

The second term $< 2 >$ and the third term $< 3 >$ of the right-hand side of (24) contain the physical boundary conditions. These are represented by the vector $\bar{W}_h$ which involves quantities that depend on the interior value W_h and quantities that are determined by the physical boundary conditions.
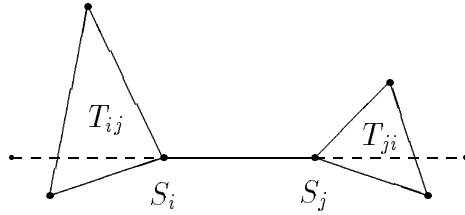
Figure 3 : Downstream and upstream triangles T_{ij} et T_{ji}

Wall boundary : the no-slip condition is taken into account using a strong formulation so that we do not need to compute the corresponding boundary integral in $< 2 >$. We make a direct use of the expressions given by (19) and (20).

Inflow and outflow boundaries : at these boundaries, a precise set of compatible exterior data which depend on the flow regime and the velocity direction, is to be specified. For this purpose a *plus-minus* flux splitting is applied between exterior data and interior values. More precisely, the boundary integral $< 3 >$ is evaluated using a non-reflective version of the flux-splitting of Steger and Warming [27] :

$$\int_{\partial C_i \cap \Gamma_\infty} \mathcal{F}(\bar{W}_h).\vec{n}_i d\sigma = \mathcal{A}^+(W_i, \vec{\nu}_{i\infty}).W_i + \mathcal{A}^-(W_i, \vec{\nu}_{i\infty}).W_\infty \qquad (37)$$

2 NUMERICAL RESULTS (COMPRESSIBLE)

2.1 Unsteady simulations

We consider here the numerical simulation of the two-dimensional low Reynolds number flow past a NACA0012 airfoil at high angle of attack and at low Mach number. Such flows have been studied in details by Pulliam [22] for several Reynolds numbers in the range [800 , 2100], for an angle of attack of 20° and a freestream Mach number of 0.2 . It is shown in [22] that when the Reynolds number increases, the unsteady flow evolves from a situation where vortices are shed periodically to a chaotic behavior. The flow conditions that we consider here are given by $M_\infty = 0.1$, $\theta = 30°$ and $Re = 1000$. Initially, the free stream conditions are assumed to prevail all over the flow. The airfoil is impulsively started in uniform flow. For the above flow conditions, similar situations as those described in [22], have been exhibited by Farhat, Fezoui and Lanteri in [7]. The computational mesh has 3114 nodes and 6056 elements.
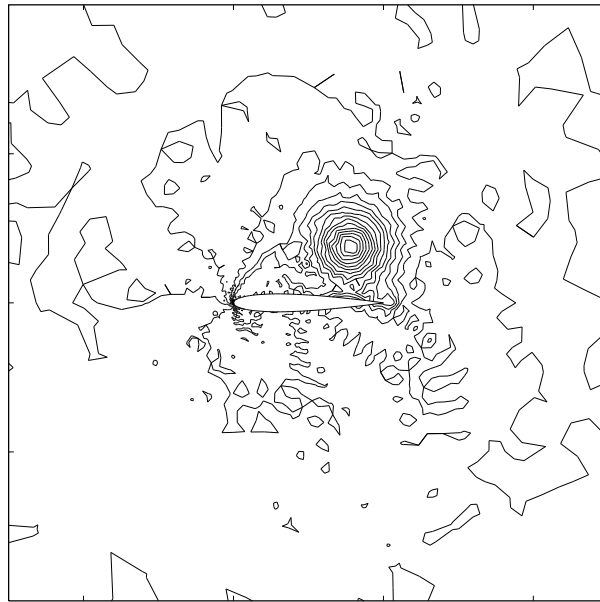
We present a number of simulation results in the form of density and Mach contours at time $t = 3$ for several of the optimal numerical schemes derived in Section 1.1. We first compare the extreme cases obtained for $\alpha = 0$, $\delta = 0$ or 1 and $\beta = \dfrac{1}{3}$; these two schemes have a small linear dispersive error (of fifth order in 1D) and essentially differ by their numerical diffusion. Results are shown on Figures 4 and 5. The centered scheme ($\delta = 0$) has clearly very good accuracy properties in the viscous part of the flow as it can be seen on the Mach contours; nevertheless, the absence of numerical diffusion in this scheme leads to the generation of spurious oscillations away from the body where the flow is convection dominated. As far as we are interested in the numerical simulation of viscous flows, the results obtained with this centered scheme can be considered as reference results for the boundary layer resolution. Conversely, the upwind scheme ($\delta = 1$) is stable but introduces too much numerical diffusion in the viscous parts of the flow.

There are several ways for decreasing the numerical diffusion introduced by the upwind scheme without loosing its stabilization properties. A first one consists in decreasing the value of the parameter β ; nevertheless, if the values of the parameters α and δ are respectively kept equal to 0 and 1 , then the obtained scheme will be dispersive. For the present simulation, characterized by a moderate value of the Reynolds number, the influence of this dispersive error term is not predominant. If we do not want to alter the dispersive properties of the scheme, then we can keep the value $\beta = \dfrac{1}{3}$ and decrease the value of the parameter δ . Figures 6 and 7 present simulation results obtained for $\delta = 1$ and $\beta = \dfrac{1}{6}$ and for $\delta = \dfrac{1}{2}$ and $\beta = \dfrac{1}{3}$. As expected from the 1D analysis no significant differences exist between the obtained simulation results.

Now, the question is: how much can we decrease the value of the parameter δ without degrading the behavior of the flow, that is without introducing spurious oscillations. The answer is clearly problem-dependent and can be partially given by considering several lower values of the parameter δ . Figures 8 and 9 present simula-

tion results obtained for $\delta = \dfrac{1}{4}$ or $\dfrac{1}{8}$ and $\beta = \dfrac{1}{3}$.

We finally present a simulation result for the modified mass matrix scheme ($\alpha = \dfrac{1}{2}$, $\delta = 1$ and $\beta = \dfrac{1}{6}$), for which the third-order dissipative error term does not depend on the value of the physical viscosity μ (there is no dependency on the value of the mesh Reynolds number in the expression (16)) of $D4$. The linear systems appearing in the time integration process (13) are approximately solved with 12 sweeps of the Jacobi iterative method. Results are shown on Figure 10. No significant improvements appear and it seems that the chosen value of the parameter α which is based on a one-dimensional study, is not suited to two-dimensional unstructured grid simulations. It would however be interesting to perform an accuracy analysis on two-dimensional structured triangular grid in order to exhibit the correct pattern for the construction of the modified matrix P_α .
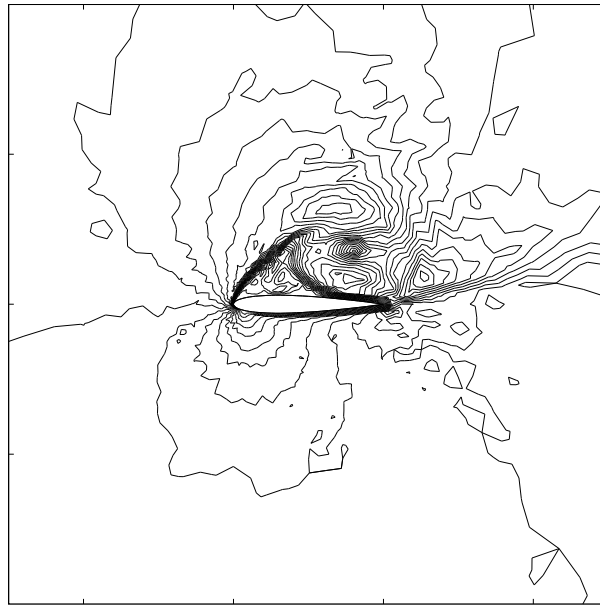
$$\alpha = 0 \quad , \quad \delta = 0 \quad , \quad \beta = \frac{1}{3} \ : \quad \rho_m = 0.963 \quad , \quad \rho_M = 1.007$$
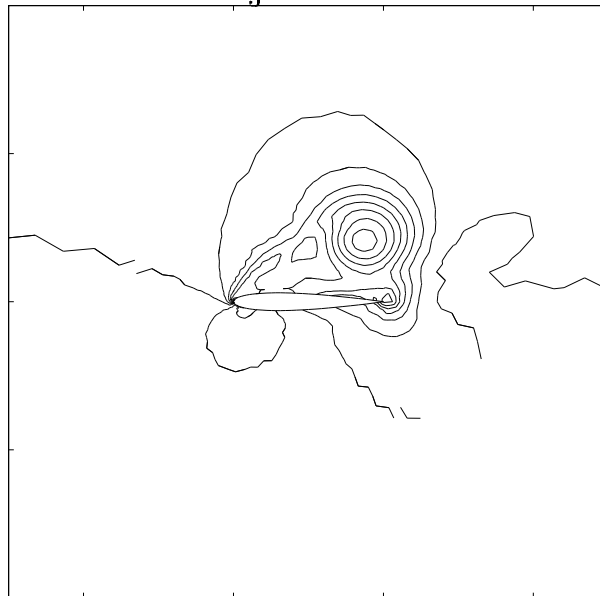
$$\alpha = 0 \quad , \quad \delta = 1 \quad , \quad \beta = \frac{1}{3} \ : \quad \rho_m = 0.980 \quad , \quad \rho_M = 1.008$$

Figure 4 : Density contours
$$\Delta\rho = 0.0025$$

$$\alpha = 0 \quad, \quad \delta = 0 \quad, \quad \beta = \frac{1}{3} : \quad M_m = 0.00 \quad, \quad M_M = 0.19$$
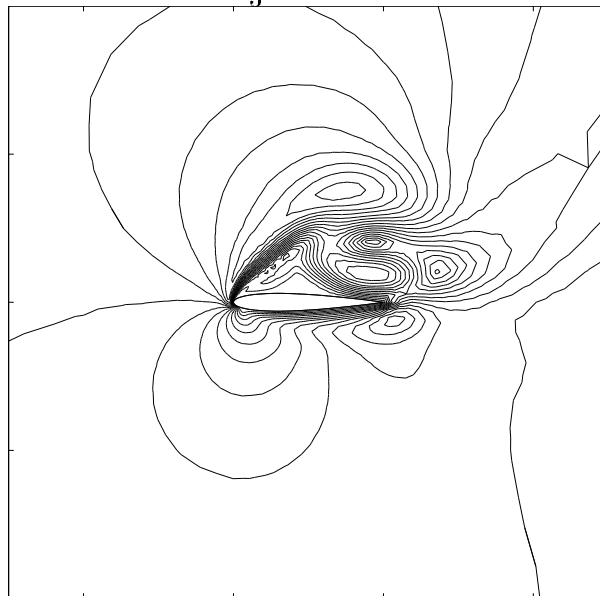
$$\alpha = 0 \quad, \quad \delta = 1 \quad, \quad \beta = \frac{1}{3} : \quad M_m = 0.00 \quad, \quad M_M = 0.17$$

Figure 5 : Mach contours
$$\Delta M = 0.01$$
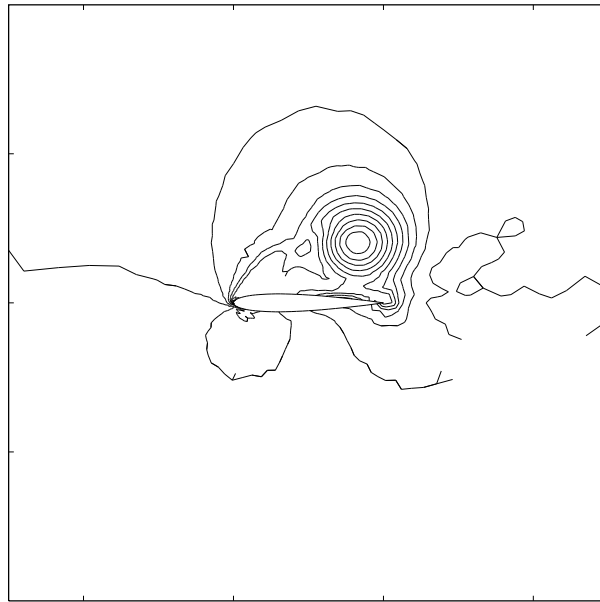
$$\alpha = 0 \quad , \quad \delta = 1 \quad , \quad \beta = \frac{1}{6} \; : \quad \rho_m = 0.975 \quad , \quad \rho_M = 1.010$$
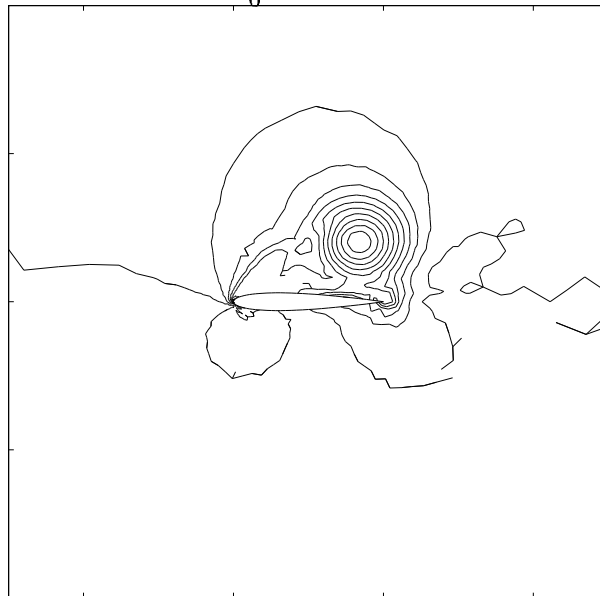
$$\alpha = 0 \quad , \quad \delta = \frac{1}{2} \quad , \quad \beta = \frac{1}{3} \; : \quad \rho_m = 0.975 \quad , \quad \rho_M = 1.008$$

Figure 6 : Density contours
$$\Delta\rho = 0.0025$$
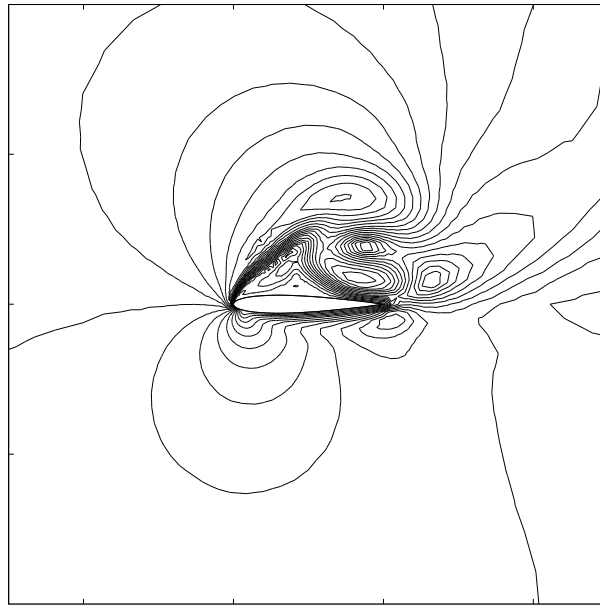
$$\alpha = 0 \quad , \quad \delta = 1 \quad , \quad \beta = \frac{1}{6} : \quad M_m = 0.00 \quad , \quad M_M = 0.18$$
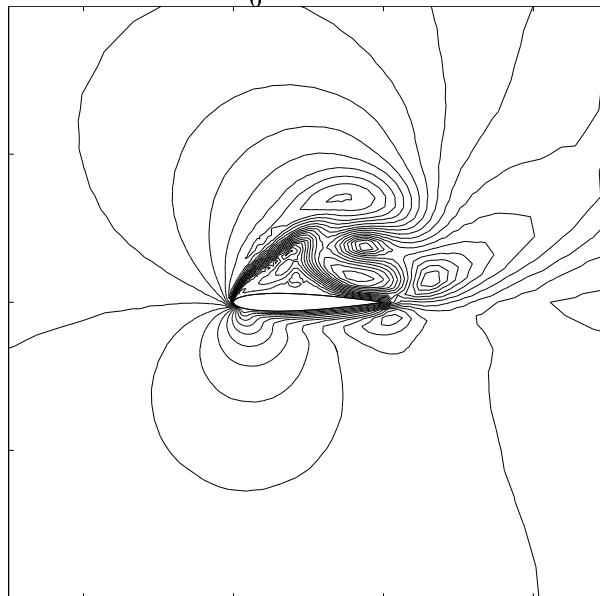
$$\alpha = 0 \quad , \quad \delta = \frac{1}{2} \quad , \quad \beta = \frac{1}{3} : \quad M_m = 0.00 \quad , \quad M_M = 0.18$$

Figure 7 : Mach contours
$$\Delta M = 0.01$$
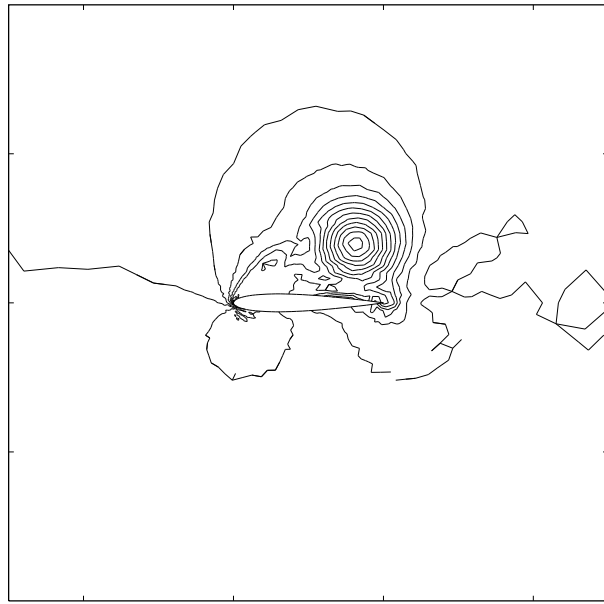
$$\alpha = 0 \quad , \quad \delta = \frac{1}{4} \quad , \quad \beta = \frac{1}{3} : \quad \rho_m = 0.970 \quad , \quad \rho_M = 1.008$$
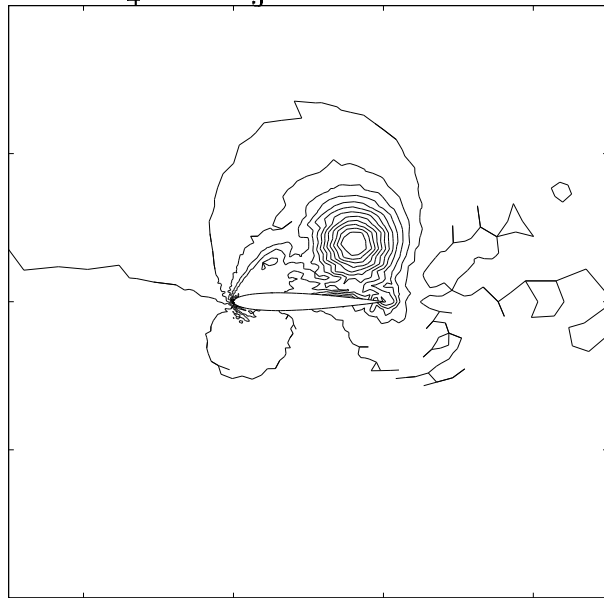
$$\alpha = 0 \quad , \quad \delta = \frac{1}{8} \quad , \quad \beta = \frac{1}{3} : \quad \rho_m = 0.970 \quad , \quad \rho_M = 1.008$$

Figure 8 : Density contours
$$\Delta \rho = 0.0025$$
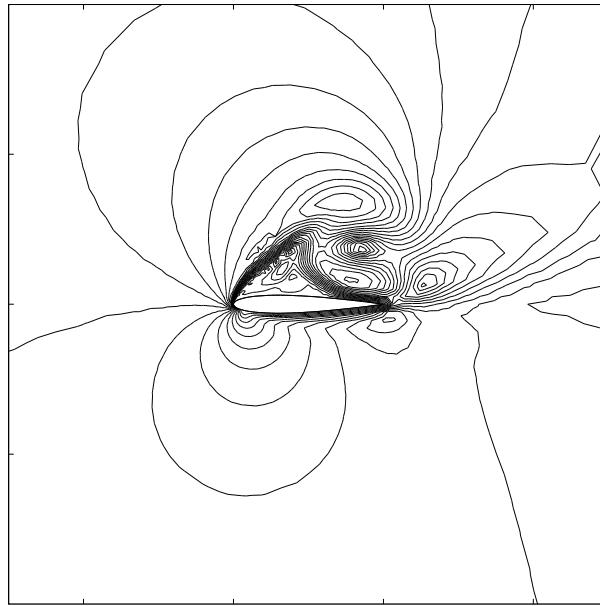
$$\alpha = 0 \quad, \quad \delta = \frac{1}{4} \quad, \quad \beta = \frac{1}{3} : \quad M_m = 0.00 \quad, \quad M_M = 0.18$$
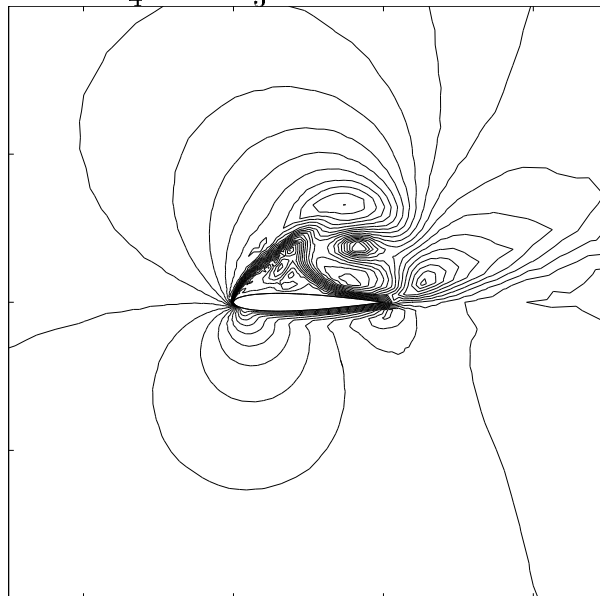
$$\alpha = 0 \quad, \quad \delta = \frac{1}{8} \quad, \quad \beta = \frac{1}{3} : \quad M_m = 0.00 \quad, \quad M_M = 0.19$$

Figure 9 : Mach contours
$$\Delta M = 0.01$$
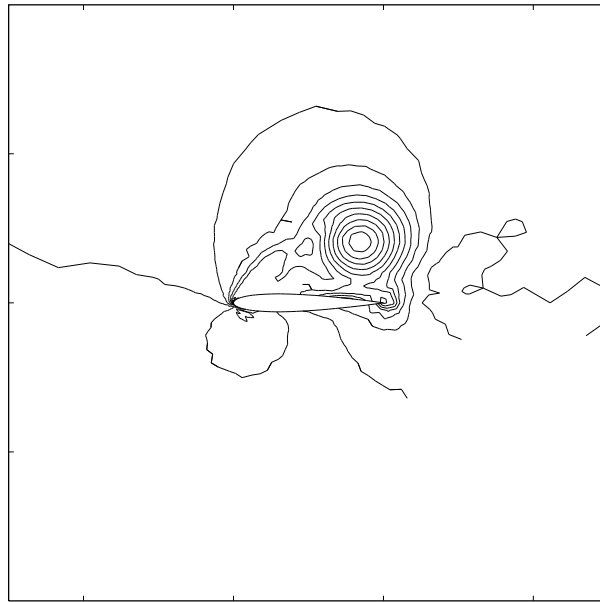
$$\alpha = \frac{1}{2} \quad , \quad \delta = 1 \quad , \quad \beta = \frac{1}{6} : \quad \rho_m = 0.975 \quad , \quad \rho_M = 1.010$$

$$\alpha = \frac{1}{2} \quad , \quad \delta = 1 \quad , \quad \beta = \frac{1}{6} : \quad M_m = 0.00 \quad , \quad M_M = 0.18$$

Figure 10 : Density and Mach contours
$$\Delta\rho = 0.0025 \quad , \quad \Delta M = 0.01$$

2.2   Steady simulations

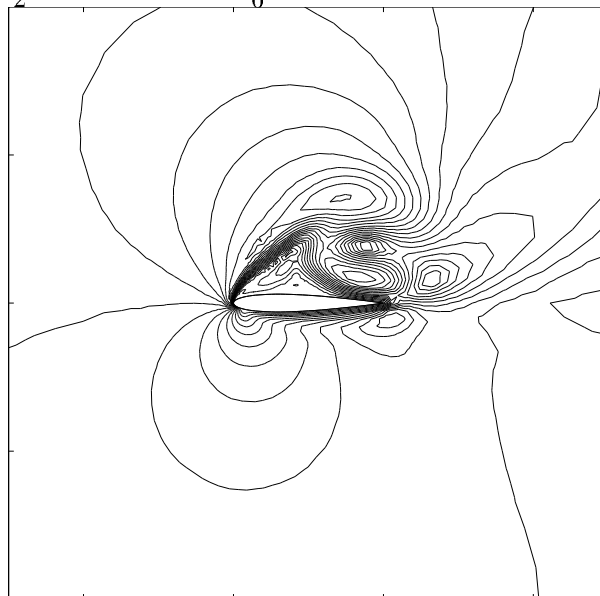We now consider the steady simulation characterized by $M_\infty = 0.85$, $\theta = 0°$ and $Re = 2000$. As the temporal approximation is of less importance in the case of steady simulations, we shall choose a scheme with good temporal dissipative properties. The dissipative properties of low storage Runge-Kutta schemes of the form (13) have been studied (among others) by Lallemand [18] in the case of the Euler equations. We shall consider here one of the schemes presented in [18] even though no similar study has been done by taking into account the diffusive fluxes.

It is a four–stage scheme :

$$
\begin{cases}
U^{(0)} & = U^n = U(t = n\Delta t) \\
\\
U^{(k)} & = U^{(0)} + \zeta_k \Delta t \Psi(U^{(k-1)}) \\
\\
& k = 1, 2, 3, 4 \\
\\
U^{(4)} & = U^{(0)} + \Delta t \Psi(U^{(4)}) = U^{n+1}
\end{cases}
\tag{38}
$$

with $\zeta_1 = 0.11$, $\zeta_2 = 0.2766$, $\zeta_3 = 0.5$ and $\zeta_4 = 1$. Note that the parameter α is equal to 0 (purely explicit scheme).

We present a number of simulation results in the form of steady–state density and Mach contours. The computational mesh used has 12286 nodes and 24224 elements.

Figures 11 and 12 give solutions for $\delta = 1$ and $\beta = \dfrac{1}{3}$; the upper solution was obtained with the original numerical flux function of Roe [24] while the lower one corresponds to the modified eigenvalues version (with an acoustic damping defined by 31-28 in Paragraph 1.2.3). Figures 13 and 14 present simulation results obtained for $\delta = 1$ and $\beta = \dfrac{1}{6}$ and for $\delta = \dfrac{1}{2}$ and $\beta = \dfrac{1}{3}$.
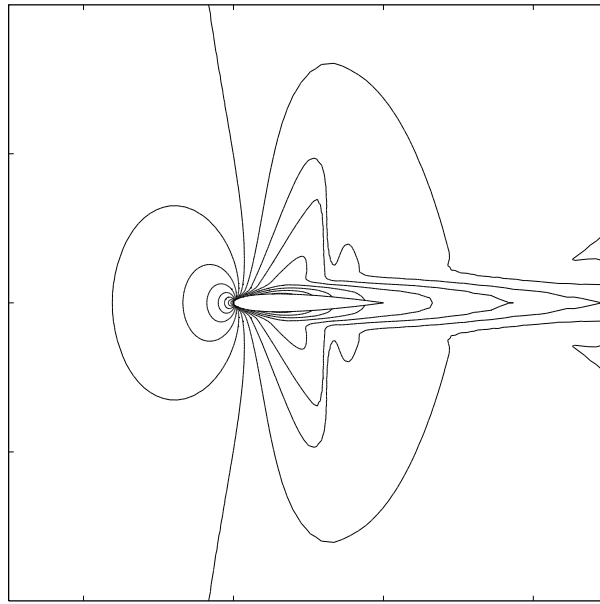
$$\delta = 1 \quad , \quad \beta = \frac{1}{3} \quad , \quad \text{Original flux} : \quad \rho_m = 0.60 \ , \ \rho_M = 1.45$$
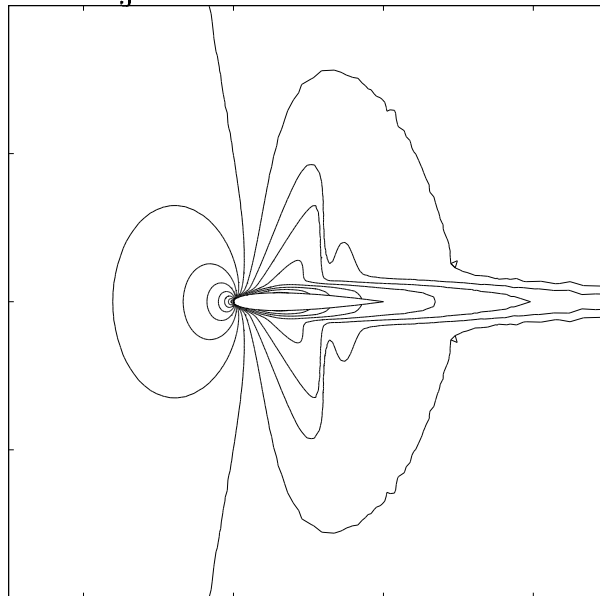
$$\delta = 0 \quad , \quad \beta = \frac{1}{3} \quad , \quad \text{Modified eingenvalues flux} : \quad \rho_m = 0.60 \ , \ \rho_M = 1.45$$

Figure 11 : Density contours
$$\Delta \rho = 0.05$$
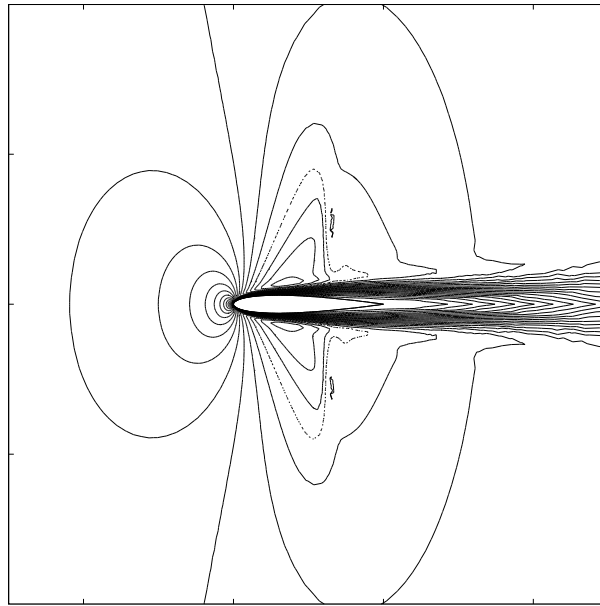
$$\delta = 1 \ \ , \ \ \beta = \frac{1}{3} \ \ , \ \ \text{Original flux}: \ \ M_m = 0.00 \ , \ M_M = 1.15$$
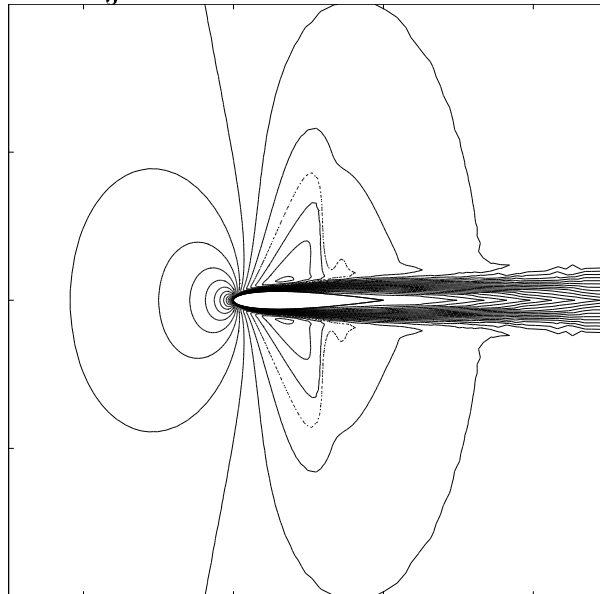
$$\delta = 0 \ \ , \ \ \beta = \frac{1}{3} \ \ , \ \ \text{Modified eingenvalues flux}: \ \ M_m = 0.00 \ , \ M_M = 1.15$$

Figure 12 : Mach contours
$$\Delta M = 0.05$$
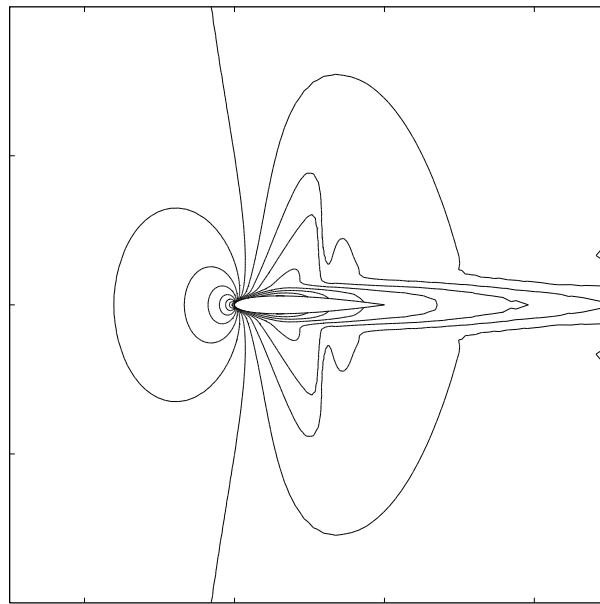
$$\delta = 1 \quad , \quad \beta = \frac{1}{6} \quad , \quad : \quad \rho_m = 0.60 \ , \ \rho_M = 1.45$$
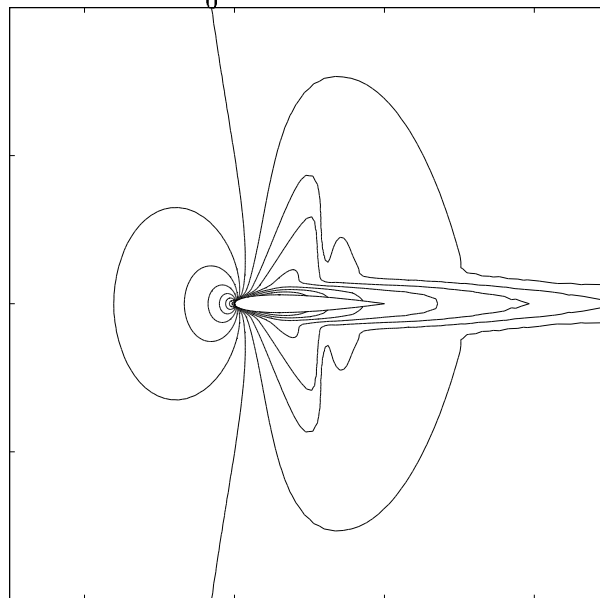
$$\delta = \frac{1}{2} \quad , \quad \beta = \frac{1}{3} \quad , \quad : \quad \rho_m = 0.60 \ , \ \rho_M = 1.45$$

Figure 13 : Density contours

$$\Delta\rho = 0.05$$
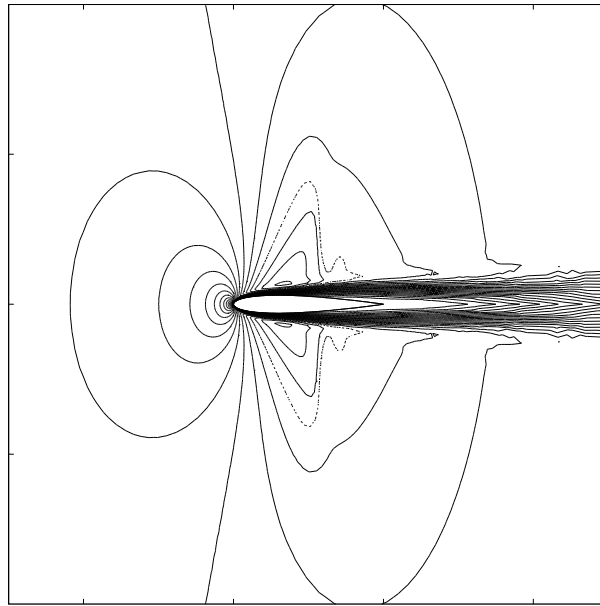
$$\delta = 1 \quad , \quad \beta = \frac{1}{6} \quad , \quad : \quad M_m = 0.00 \ , \ M_M = 1.15$$
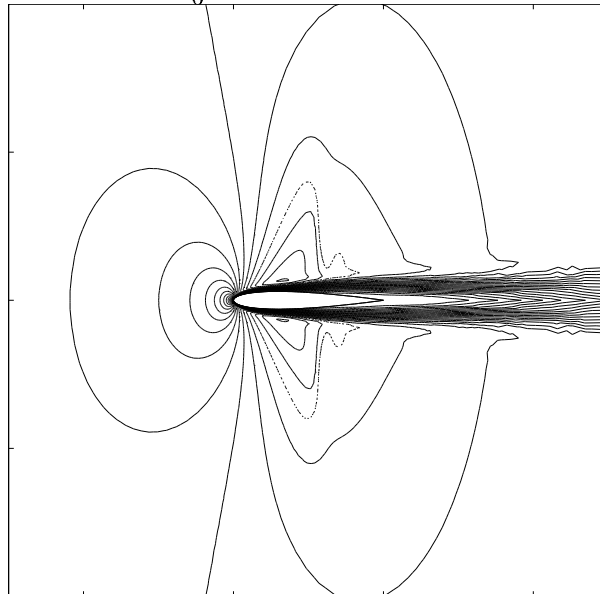
$$\delta = \frac{1}{2} \quad , \quad \beta = \frac{1}{3} \quad , \quad : \quad M_m = 0.00 \ , \ M_M = 1.15$$

Figure 14 : Mach contours
$$\Delta M = 0.05$$

3 AN UPWIND SCHEME FOR INCOMPRESSIBLE FLOW

We now present and discuss some upwind schemes for the simulation of incompressible flows. These schemes are based on the **artificial compressibility** approximation (this approach is now well-known, we refer to e.g. [6] for recent applications and further references).

The different hyperbolic system which appear below in the framework of the artificial compressibility approximation are analysed and discussed in detail in Appendix 1.

3.1 Steady incompressible flow with constant density

Let us first consider now a steady two-dimensional incompressible flow with the density assumed constant. Then the Navier-Stokes equations can be written in the following way, u and v denoting the velocity components and p the pressure :

$$\begin{cases} uu_x + vu_y + p_x = \nu\Delta u \ , \\[2mm] uv_x + vv_y + p_y = \nu\Delta v \ , \\[2mm] u_x + v_y = 0 \ . \end{cases} \tag{39}$$

The artificial compressibility approximation consists in subtituting the following equation $p_t + k^2(u_x + v_y) = 0$, where k is a positive constant, for the incompressibility condition $u_x + v_y = 0$. Thus, we consider the following system :

$$\begin{cases} u_t + (u^2 + p)_x + (uv)_y = \nu\Delta u \ , \\[2mm] v_t + (uv)_x + (v^2 + p)_y = \nu\Delta v \ , \\[2mm] p_t + k^2(u_x + v_y) = 0 \ , \end{cases} \tag{40}$$

which we write as:

$$W_t + F(W)_x + G(W)_y = R.H.S. \ , \tag{41}$$

where the right-hand side consists of the viscous terms, and where:

$$W = \begin{pmatrix} u \\ v \\ p \end{pmatrix} \ , \quad F(W) = \begin{pmatrix} u^2 + p \\ uv \\ k^2 u \end{pmatrix} \ , \quad G(W) = \begin{pmatrix} uv \\ v^2 + p \\ k^2 v \end{pmatrix} \ . \tag{42}$$

This system is known to be hyperbolic. For any vector $\vec{\eta} = (\eta_x, \eta_y)$, the Jacobian matrix $\quad A(W, \vec{\eta}) = \eta_x \dfrac{\partial F(W)}{\partial W} + \eta_y \dfrac{\partial G(W)}{\partial W} \quad$ can be diagonalized in the form $A =$

$T\Lambda T^{-1}$, where T is the matrix of the right eigenvectors of A, and where:

$$\Lambda = \begin{pmatrix} \lambda_0 & 0 & 0 \\ 0 & \lambda_0 + \tau & 0 \\ 0 & 0 & \lambda_0 - \tau \end{pmatrix} , \tag{43}$$

with $\quad \lambda_0 = \vec{V}.\vec{\eta} = \eta_x u + \eta_y v$ and $\tau = \sqrt{\lambda_0^2 + k^2 \parallel \vec{\eta} \parallel^2}$.

We can then define a Q-scheme for the approximation of system (40), as proposed by Harten, Lax and Van Leer [15]. The numerical scheme for the solution of this system is then very similar to the scheme used for compressible flows in the previous section. The numerical flux function for the hyperbolic part writes:

$$\Phi^R(U,V,\vec{\eta}) = \frac{\mathcal{F}(U,\vec{\eta}) + \mathcal{F}(V,\vec{\eta})}{2} - \frac{1}{2} |A(\frac{U+V}{2},\vec{\eta})| \, (V - U) , \tag{44}$$

with $\mathcal{F}(W,\eta) = \eta_x F(W) + \eta_y G(W)$. Since the fluxes F and G are quadratic, it is easy to see that the numerical flux (44) is in fact a Roe scheme for system (40), because the following property holds for any pair (W_L, W_R):

$$A(\frac{W^R + W^L}{2},\vec{\eta})(W^R - W^L) = \mathcal{F}(W^L,\vec{\eta}) - \mathcal{F}(W^R,\vec{\eta}) .$$

3.2   Steady incompressible flow with non constant density

We now the above scheme to a model of incompressible flow where the density ρ, is not constant; such a scheme enables us to study a flow for two fluids with different densities. For a steady flow, the model writes as follows:

$$\begin{cases} u\rho_x + v\rho_y = 0 , \\[2mm] \rho u u_x + \rho v u_y + p_x = \nu \Delta u , \\[2mm] \rho u v_x + \rho v v_y + p_y = \nu \Delta v , \\[2mm] u_x + v_y = 0 . \end{cases} \tag{45}$$

Using again the artificial compressibility approximation, we will consider the following system :

$$
\begin{cases}
\rho_t + (\rho u)_x + (\rho v)_y = 0 \; , \\[2mm]
(\rho u)_t + (\rho u^2 + p)_x + (\rho u v)_y = \nu \Delta u \; , \\[2mm]
(\rho v)_t + (\rho u v)_x + (\rho v^2 + p)_y = \nu \Delta v \; , \\[2mm]
p_t + k^2(u_x + v_y) = 0 \; ,
\end{cases}
\tag{46}
$$

and introduce the vector form:

$$
W_t + F(W)_x + G(W)_y = R.H.S. \; , \tag{47}
$$

where the right-hand side again consists of the viscous terms, and where:

$$
W = \begin{pmatrix} \rho \\ \rho u \\ \rho v \\ p \end{pmatrix} \; , \quad
F(W) = \begin{pmatrix} \rho u \\ \rho u^2 + p \\ \rho u v \\ k^2 u \end{pmatrix} \; , \quad
G(W) = \begin{pmatrix} \rho v \\ \rho u v \\ \rho v^2 + p \\ k^2 v \end{pmatrix} \; . \tag{48}
$$

As in the previous case, we obtain here an hyperbolic system. For any vector $\vec{\eta} = (\eta_x, \eta_y)$, the Jacobian matrix $A(W, \vec{\eta}) = \eta_x \dfrac{\partial F(W)}{\partial W} + \eta_y \dfrac{\partial G(W)}{\partial W}$ is diagonalisable; it can be written on the form $A = T \Lambda T^{-1}$, with:

$$
\Lambda = \begin{pmatrix}
\lambda_0 & 0 & 0 & 0 \\[2mm]
0 & \lambda_0 & 0 & 0 \\[2mm]
0 & 0 & \dfrac{\lambda_0}{2} + \tau & 0 \\[3mm]
0 & 0 & 0 & \dfrac{\lambda_0}{2} - \tau
\end{pmatrix} \; , \tag{49}
$$

where $\lambda_0 = \vec{V}.\vec{\eta} = \eta_x u + \eta_y v$ and $\tau = \sqrt{\dfrac{\lambda_0^2}{2} + \dfrac{k^2}{\rho} \parallel \vec{\eta} \parallel^2}$.

Following the same lines as above, we can easily define a Q-scheme for the approximation of system (46), using the expression (44).

4   NUMERICAL TESTS : SQUARE WALL DRIVEN CAVITY FLOW

4.1   Geometrical data

We consider an incompressible steady flow in a square cavity, the top wall of which moves with an uniform velocity. It is a classical model problem for testing and evaluating numerical methods. The corresponding geometry is defined in the following Figure 15.
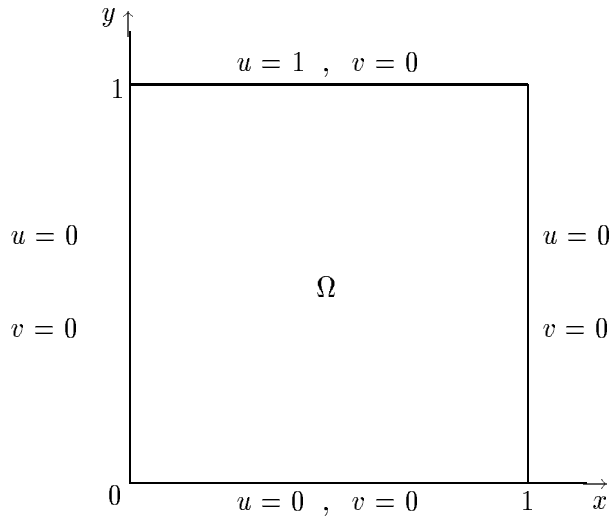
Figure 15 : Geometry and boundary conditions of the square wall driven cavity flow

4.2   Incompressible flow results

For this test case, we compare the results for Reynolds number equal to 400 and 1000. We have used here an implicit scheme with a spatial second-order accuracy.
First we are interested on the variation along the centre line $x = 0.5$ of the horizontal component of the velocity. In Figure 16, we plot, for a Reynolds number equal to 1000, the evolution of the solution with the mesh's refinement. The solutions are converged at eight orders of magnitude for the 121-nodes and 441-nodes meshes, at seven orders for the 1681-nodes mesh and at five orders for the 4625-nodes one.
We present in Figure 17 a comparison between our work with our finer mesh (4625 nodes) and different studies for Re=1000: the works of Ghia et al. [13] (1982), FDM without upwinding and 128 x 128 nodes, Nallasamy et al. [20] (1977), FDM with upwinding and 50 x 50 nodes, Kondo et al. [17] (1988) with FEM third-order upwinding and 40 x 40 nodes, Tabata at al. [28] (1988) with FEM third-order upwinding and 24 x 24 nodes. We can observe a good agreement particulary with Ghia et al. which have

employed the finer mesh.

In the same way, we compare, for Re=400, our results computed with an 1681-nodes mesh and different works using centered schemes and few nodes (except for Burggraf [2] who have 40 x 40 nodes) [29]. The comparison is plotted in Figure 18.

We present now a succession of comparison between Tuann and Olson's results [30] (1977) and our results with an 1681-nodes mesh on isobaric lines and lines of constant velocity for Reynold number equal to 400 and 1000. Tuann and Olson use a finite element mesh with 85 vertices and 132 triangular elements; each element has 18 degrees of freedom for the streamfunction interpolation.

The solutions are plotted in Figures 19 (Tuann and Olson) and 20 for Re=400, and in Figures 24 (Tuann and Olson) and 23 for Re=1000. Notice that for the isobaric lines we have take $P = P - P_r$ where P_r is the pressure at the centre of the bottom wall of the cavity in order to can compared with Tuann et al. But we do not have the same normalisation of the pressure. So only the isoline equal to zero corresponds exactly in the both cases.

For isovorticity's lines, we compare with the centered finite element method of Fortin, Peyret and Temam [10]. We notice that in the presented study we use an uniform 1681-nodes mesh as in [10]. The same values of isovorticity are used for our solution and the Fortin, Peyret and Temam one (see Figures 21, 22 for Re=400 and 25, 26 for Re=1000).
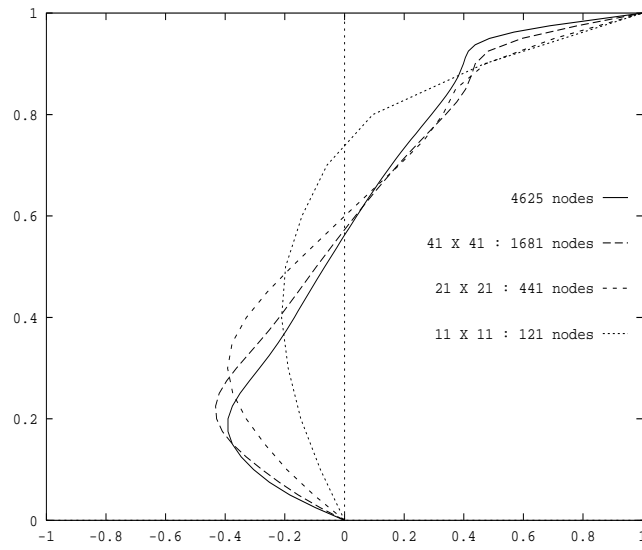
Figure 16 : Re = 1000 : Profile of horizontal velocity along vertical centre line : Different meshes

Figure 17 : Re = 1000 : Profile of horizontal velocity along vertical centre line : Comparison with others results

Figure 18 : Re = 400 : Profile of horizontal velocity along vertical centre line

Figure 19 : Tuann and Olson : isobaric lines (on the left) and lines of constant velocity (on the right) for Re = 400
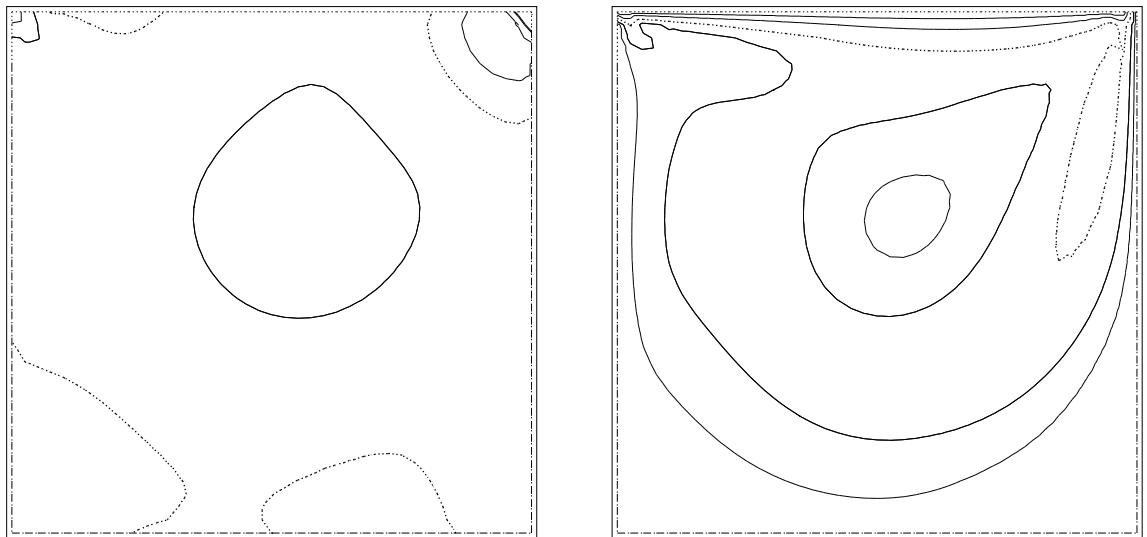
Figure 20 : Isobaric lines (on the left) and lines of constant velocity (on the right) for Re = 400 (1681-nodes mesh)

Figure 21 : Fortin, Peyret, Temam : Lines of equivorticity for Re = 400 (41 x 41 nodes mesh)
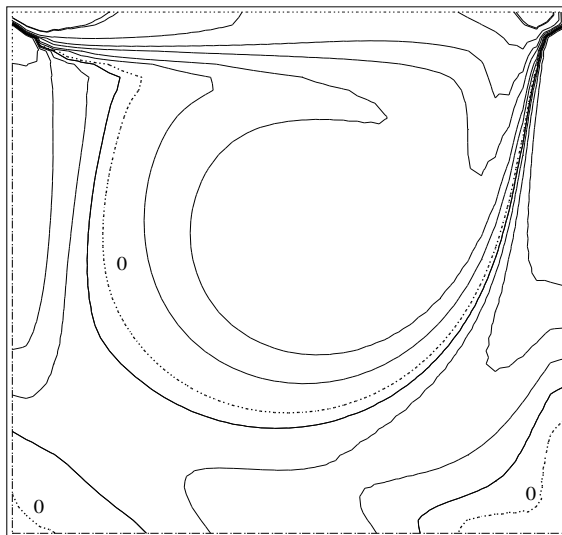
Figure 22 : Lines of equivorticity for Re = 400 (41 x 41 nodes mesh)

Figure 23 : Tuann and Olson : isobaric lines (on the left) and lines of constant velocity (on the right) for Re = 1000
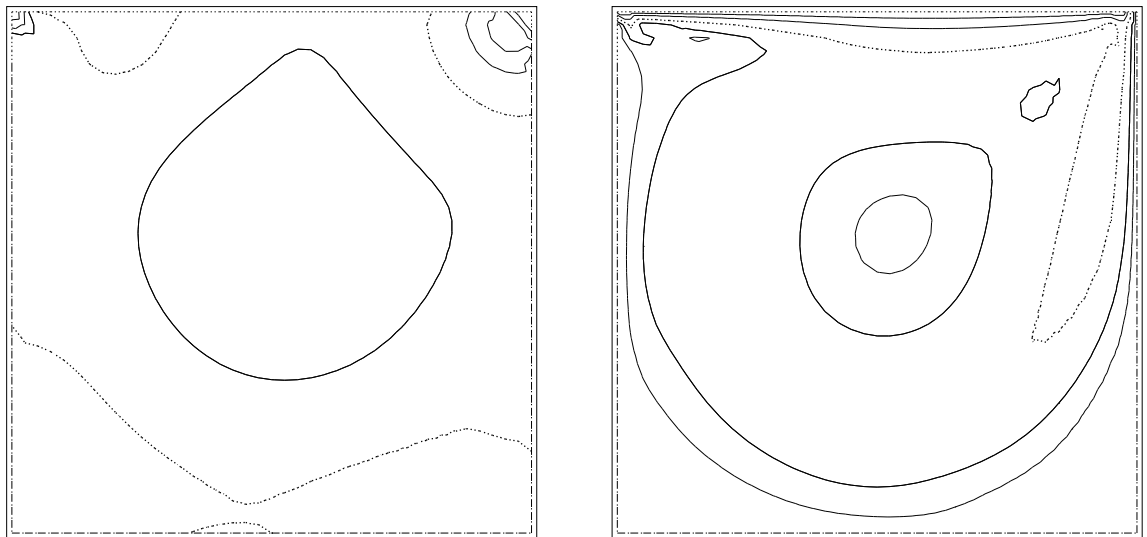
Figure 24 : Isobaric lines (on the left) and lines of constant velocity (on the right) for Re = 1000 (1681-nodes mesh)

Figure 25 : Fortin, Peyret, Temam : Lines of equivorticity for Re = 1000 (41 x 41 nodes mesh)
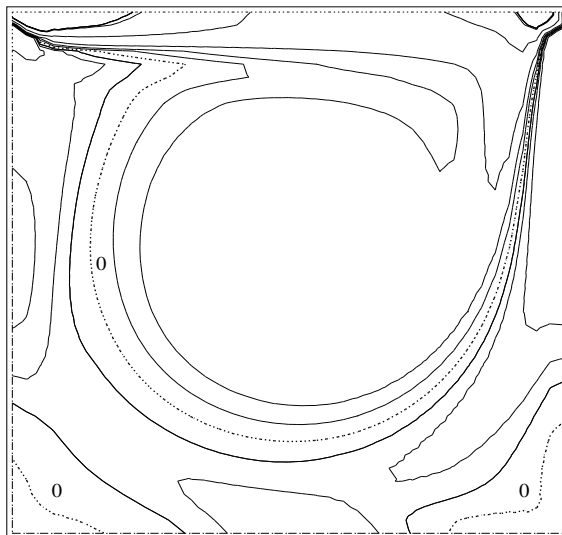
Figure 26 : Lines of equivorticity for Re = 1000 (41 x 41 nodes mesh)

4.3 A centered-upwind approach

In order to study the effect of the numerical diffusion on stabilisation of advective and pressure terms, we deduce from the Harten Van Leer flux function defined in Section 3 a partly-upwind approximation. In this way, we introduce a matrix $\tilde{K}$, which in Section 3 and Paragraph 4.2 is the identity operator, and defined by the following expression :

$$\tilde{K} \ = \ T \ \begin{pmatrix} 0 & 0 & 0 \\ 0 & 1 & 0 \\ 0 & 0 & 1 \end{pmatrix} \ T^{-1}$$

The flux is then given by :

$$\tilde{\Phi}(U, V, \vec{\eta}) = \frac{\mathcal{F}(U, \vec{\eta}) + \mathcal{F}(V, \vec{\eta})}{2} - \frac{1}{2} \tilde{K} T \left| \Lambda \right| T^{-1} (V - U)$$

$\tilde{\Phi}$ defined previously corresponds in fact to the modified flux function of Roe $\tilde{\Phi}_{\mathcal{F}}^{\delta}$ defined in the compressible case (see relations (31), (32) in Paragraph "Acoustic damping" of Section 1.2). We can notice that we have not consider, here, any weight coefficients, i.e. we are in the case $\delta = 1$.

The purpose of the two following paragraphs is to numerically investigate whether this new partly-upwind approximation is a stable one at low mesh Reynolds numbers. We present comparisons between fully upwind schemes and partly-upwind ones.

The mesh used is an uniform triangular 41×41 nodes mesh.

4.3.1 First-order accurate experiments

We use an explicit scheme with a spatial first-order accuracy and with a time integration performed using a four-stage low-storage Runge Kutta scheme. The Runge-Kutta coefficients are given by:

$\zeta_1 = 0.11$, $\zeta_2 = 0.2766$, $\zeta_3 = \dfrac{1}{2}$, $\zeta_4 = 1$

For a Reynolds number equal to 1000, we compare the obtained results with the partly-upwinding scheme and the initial one.

The different solutions are converged at six orders of magnitude.

We compare the both experiments and first-order results obtained by Tabata et al [28] in Figure 27 where is plotted the first component of the velocity in function of y for $x = 0.5$. We note a great difference with the second-order accuracy results (see Figures 16 and 17), and in fact, just a slight difference between both first-order accurate schemes.

Figure 27 : Re = 1000: Profile of horizontal velocity along vertical centre line (dashed line for initial scheme and solid line for partly-upwinding one)

4.3.2   Second-order accurate experiments

In order to obtain a spatial second-order accuracy we use an explicit β-scheme and so we choose the Runge Kutta coefficients in function of β (see the 1-D analysis in Appendix 2 below) :

$$\zeta_1 = 0.166 \,, \; \zeta_2 = 0.307 \,, \; \zeta_3 = \tfrac{1}{2} \,, \; \zeta_4 = 1 \; \text{ for } \beta = \tfrac{1}{3}$$

$$\zeta_1 = 0.199 \,, \; \zeta_2 = 0.312 \,, \; \zeta_3 = \tfrac{1}{2} \,, \; \zeta_4 = 1 \; \text{ for } \beta = \tfrac{1}{6}.$$

We take a Reynolds number equal to 100 and we search a solution converged at five orders of magnitude.

We compare the results obtained if we put to zero the eigenvalue corresponding at the advective part of the numerical diffusion with the original ones, and this for two values of β : $\dfrac{1}{6}$, $\dfrac{1}{3}$. We compare too with Tuann and Olson results [30] (see the previous paragraph 4.2) and isobaric lines and lines of constant velocity are plotted for all theses different cases.

We obtain a good accordance with the references results (Figures 28, 29). With this low Reynolds number, we can not distinguish between the results obtained with the partly-upwinding scheme (Figures 30, 32) and the initial one (Figures 31, 33). The experiments with $\beta = \dfrac{1}{3}$ seems to be less perturbed.

Figure 28 : Tuann and Olson : isobaric lines for Re = 100

Figure 29 : Tuann and Olson : Lines of constant velocity for Re = 100

Figure 30 : Re = 100 : $\beta = \frac{1}{3}$ $CFL = 0.55$ isobaric lines (on the left) and lines of constant velocity (on the right)

Figure 31 : Re = 100 : $\beta = \frac{1}{3}$ $CFL = 0.55$ with modified eigenvalues   isobaric lines (on the left) and lines of constant velocity (on the right)
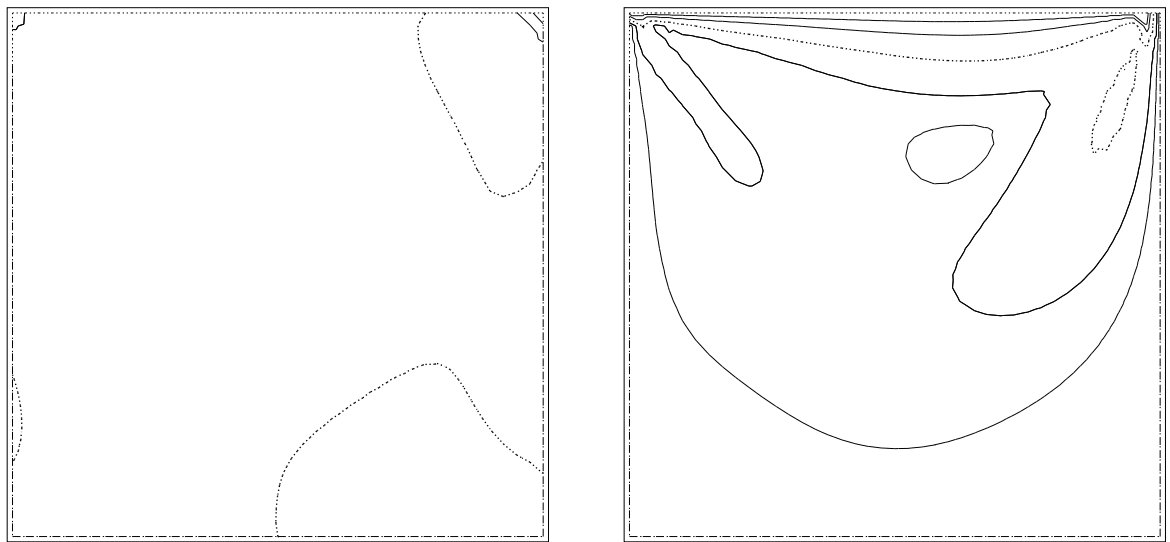
Figure 32 : Re $= 100$: $\beta = \frac{1}{6}$ $CFL = 0.6$ isobaric lines (on the left) and lines of constant velocity (on the right)
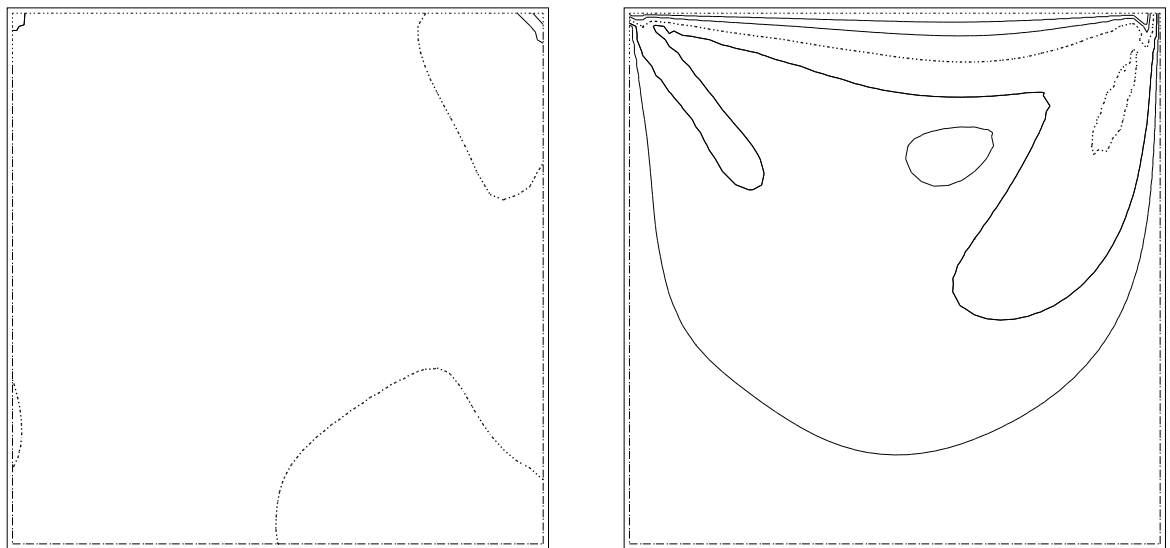

Figure 33 : Re $= 100$: $\beta = \frac{1}{6}$ $CFL = 0.6$ with modified eigenvalues isobaric lines (on the left) and lines of constant velocity (on the right)
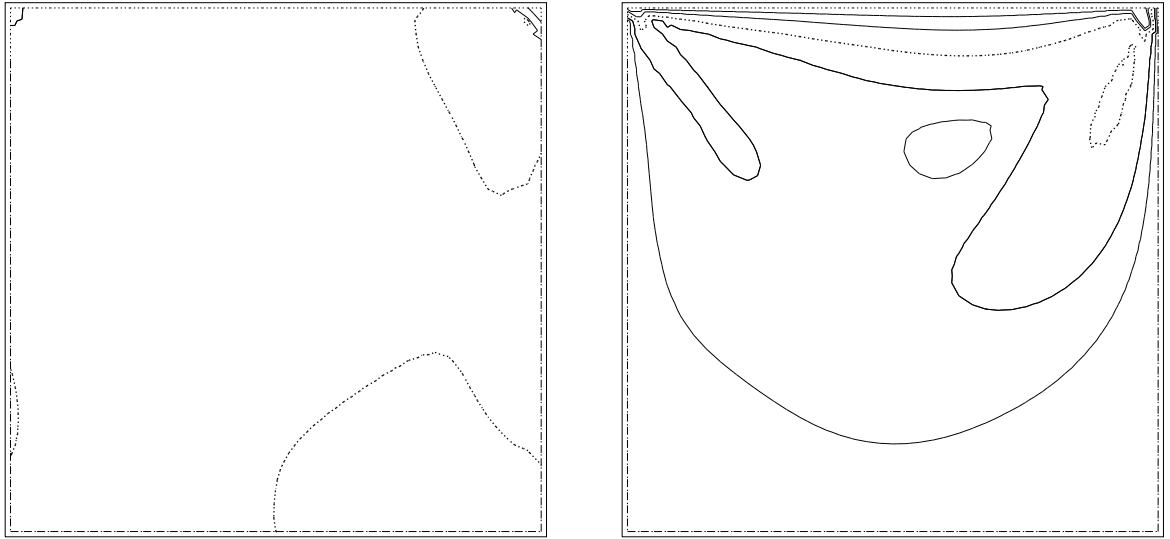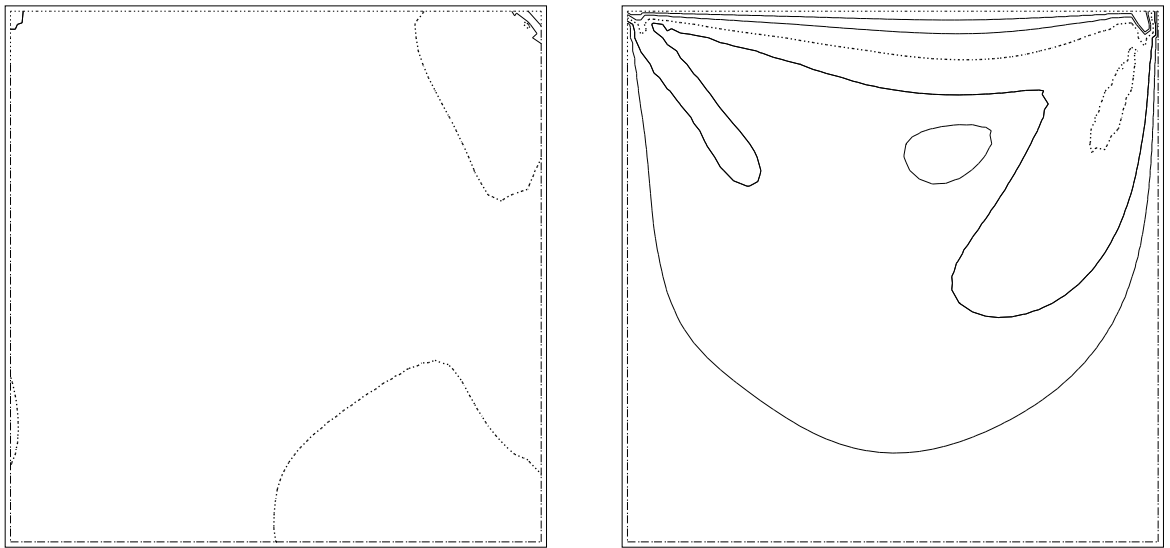
5   CONCLUSION

In this work, we have put both incompressible and compressible fluid models in a hyperbolic frame. This allowed to propose a family of upwind schemes relying on Flux-Difference-Splitting and a FEM/FVM formulation for unstructured meshes. The resulting MUSCL-FEM schemes are formally second-order accurate for all independent variables, but both involve yet too much numerical viscosity.

Indeed, in the case of subsonic flows, we have exhibited improved accuracy for versions that are less upwinded; those versions could be cast in a large family of schemes that could be third-order or even fourth-order accurate in the one-dimensional uniform-meshed case.

It should be noted that the same remarks could be done for both incompressible and compressible cases: in both cases exist two kinds of first-order derivatives, advection terms and isotropic ones involved in the pressure and continuity-equation ones. In the case of subsonic flows, it seems that different treatments for these two types of terms should bring some improvement. In this paper, we have noted that viscous terms could stabilize (essentially but not completely) advection.

Then our point of view consists of trying to reduce numerical dissipation by reducing the upwinding of advection terms through a modification of the flux-difference splitting. This point of view was also implemented in a semi-implicit context by Guillard and Fernandez [8] in which the implicit dissipation did not apply to advection for saving accuracy. In our study, the corresponding artificial viscosity could be switched off without loss of stability, but the accuracy improvement has been rather disappointing.

Therefore this study calls sequels: while shocks still need first-order characteritic upwinding, regular parts of the flow could much better approximated by finding stabilizing terms addressing advection and acoustics separately; from this point of view, new flux splitting are to be derived. Also, the level of upwinding and the switch to shock-capturing fluxes have to be cleverly monitored.

A   Appendix 1

We analyse and discuss in this appendix the different hyperbolic systems which arose in Section 3.1 in the framework of the constant density approximation.

Let us begin with a general remark: the investigation of these hyperbolic systems is of interest for a better understanding of the upwind numerical methods used in this work. But it is important to keep in mind that these system are not correct from the physical point of view, since they are based on the artificial compressibility approach. As a consequence, their solution will sometimes exhibit some unusual behaviour. As an example, it will appear that the simplest system (50) below does have solutions with shock waves propagating at any non zero speed s, but cannot have a solution with a steady shock wave ! This strange fact is only possible because the artificial compressibility breaks the galilean invariance of the original system which describes the flow.

A.1   One-dimensional flow with constant density

We examine here the solution of a Riemann problem for the one-dimensional system:

$$\begin{cases} u_t + (u^2 + p)_x = 0 \ , \\ p_t + k^2 u_x = 0 \ , \end{cases} \tag{50}$$

taken from the system (40) obtained by the artificial compressibility approach.

Setting:

$$W = \begin{pmatrix} u \\ p \end{pmatrix} \ , \quad F(W) = \begin{pmatrix} u^2 + p \\ k^2 u \end{pmatrix} \ , \tag{51}$$

and considering two states W_L and W_R, we consider the Riemann problem:

$$\begin{cases} W_t + F(W)_x = 0 \quad \text{for } x \in I\!\!R \ , \quad t \geq 0 \ , \\ \\ W(x,0) = \begin{cases} W_L & \text{if } x < 0 \ , \\ W_R & \text{if } x > 0 \ . \end{cases} \end{cases} \tag{52}$$

The Jacobian matrix:

$$A(W) = \frac{\partial F}{\partial W} = \begin{pmatrix} 2u & 1 \\ k^2 & 0 \end{pmatrix} \tag{53}$$

has two real eigenvalues $\lambda_1 = u - \sqrt{k^2 + u^2}$ and $\lambda_2 = u + \sqrt{k^2 + u^2}$, which are respectively associated with the two following right eigenvectors:

$$r_1 = \begin{pmatrix} -1 \\ \lambda_2 \end{pmatrix} \ , \quad r_2 = \begin{pmatrix} -1 \\ \lambda_1 \end{pmatrix} \ . \tag{54}$$

The problem is strictly hyperbolic since $\lambda_1 < \lambda_2$, and both characteristic fields are **genuinely nonlinear**, since :

$$\nabla\lambda_1.r_1 = -\frac{\partial\lambda_1}{\partial u} = -1 + \frac{u}{\sqrt{k^2 + u^2}} < 0 \ ,$$

$$\nabla\lambda_2.r_2 = -\frac{\partial\lambda_2}{\partial u} = -1 - \frac{u}{\sqrt{k^2 + u^2}} < 0 \ .$$

Thus, we know from the general theory about hyperbolic problems (see e.g. Lax [19], Smoller [26]) that the Riemann problem (52) has a unique solution if the two states W_L and W_R are close enough to each other. This solution consists of 3 constants states: W_L, W^* and W_R, with either a 1-shock or a 1-rarefaction between W_L and W^*, and either a 2-shock or a 2-rarefaction between W^* and W_R.

We will construct this solution below, assuming that the reader has some familiarity with the above references [19, 26].

A.1.1   Rarefaction waves

Let us investigate more precisely the rarefaction waves. In such a wave, $W(x,t)$ only depends on the ratio $\sigma = \dfrac{x}{t}$: we write: $W(x,t) = V(\sigma)$. Moreover, since W is continuously differentiable in a rarefaction wave, we have $W_t + A(W)W_x = 0$, from which we deduce that:

$$A(V(\sigma))V'(\sigma) = \sigma V'(\sigma) \ .$$

For a 1-rarefaction, this relation implies that $V'(\sigma)$ is colinear with $r_1(V(\sigma))$ and that $\lambda_1(V(\sigma)) = \sigma$. Differentiating the latter relation with respect to σ , we obtain $\nabla\lambda_1.V'(\sigma) = 1$, whence:

$$V'(\sigma) = \begin{pmatrix} u'(\sigma) \\ p'(\sigma) \end{pmatrix} = \frac{1}{\nabla\lambda_1.r_1} r_1 = \begin{pmatrix} -\dfrac{\sqrt{k^2 + u^2}}{\lambda_1} \\ \dfrac{\lambda_2}{\lambda_1}\sqrt{k^2 + u^2} \end{pmatrix} \ . \tag{55}$$

This is the equation of the so-called "integral curve" for a 1-rarefaction. Since $u'(\sigma)$ does not vanish, we can write:

$$p(u) = -\int^u \lambda_2(v)\, dv = -\int^u (v + \sqrt{v^2 + k^2})\, dv \ . \tag{56}$$

We can evaluate this integral using the change of variable $x = \log\left(\dfrac{v + \sqrt{v^2 + k^2}}{k}\right)$ (i.e. $v = k\sinh x$). Setting:

$$\phi_1(u, p) = p + \frac{u^2}{2} + \frac{u}{2}\sqrt{u^2 + k^2} + \frac{k^2}{2}\log\left(\frac{u + \sqrt{u^2 + k^2}}{k}\right) \ , \tag{57}$$

we obtain the following result: the state $W = (u, p)^T$ can be linked to the state $W_L = (u_L, p_L)^T$ by a 1-rarefaction, with W_L on the left of the rarefaction wave, if and only if:

$$\phi_1(W) = \phi_1(W_L) \quad \text{and} \quad u > u_L \ . \tag{58}$$

In other words, ϕ_1 is a 1-Riemann invariant for our system.

In the same way, we easily obtain the following. Setting:

$$\phi_2(u, p) = p + \frac{u^2}{2} - \frac{1}{2}u\sqrt{u^2 + k^2} - \frac{k^2}{2}\log\left(\frac{u + \sqrt{u^2 + k^2}}{k}\right) \ , \tag{59}$$

a state $W = (u, p)^T$ can be linked to the state $W_R = (u_R, p_R)^T$ by a 1-rarefaction, with W_R on the right of the rarefaction wave, if and only if:

$$\phi_2(W) = \phi_2(W_L) \quad \text{and} \quad u < u_R \ . \tag{60}$$

A.1.2   Shock waves

After the rarefaction waves, we want now to study the shock waves. Assuming that a 1-shock wave propagating with the speed s separates the states $W_L = (u_L, p_L)^T$ and $W = (u, p)^T$, with W_L on the left of the shock, we can write the Rankine-Hugoniot relations:

$$\begin{cases} (u^2 + p) - (u_L^2 + p_L) = s(u - u_L) \ , \\[2mm] k^2(u - u_L) = s(p - p_L) \ , \end{cases} \tag{61}$$

and the entropy inequalities:

$$u_L - \sqrt{k^2 + u_L^2} > s > u - \sqrt{k^2 + u^2} \ , \quad u + \sqrt{k^2 + u^2} > s \ . \tag{62}$$

We easily see that the first two inequalities in (62) impose that $u < u_L$ and $s < 0$, which shows that the last inequality in (62) always holds. Since $s \neq 0$, we can deduce from (61) that:

$$u + u_L = s - \frac{k^2}{s} \ ,$$

whence:

$$s = \frac{u + u_L}{2} - \sqrt{k^2 + (\frac{u + u_L}{2})^2} \ . \tag{63}$$

Now, we see that, if s is given by (63) and if $u < u_L$, then all inequalities (62) are fulfilled. Using this value of s in the second relation (61), we obtain that, finally, the state W must satisfy:

$$p = p_L + (u_L - u)\left[\frac{u + u_L}{2} + \sqrt{k^2 + \left(\frac{u + u_L}{2}\right)^2}\right] \tag{64}$$

With similar arguments, we can show that a 2-shock wave necessarily propagates with a positive speed, and that it separates the states $W = (u, p)^T$ and $W_R = (u_R, p_R)^T$, with W_R on the right of the shock, if and only if:

$$p = p_R + (u_R - u) \left[\frac{u + u_R}{2} - \sqrt{k^2 + \left(\frac{u + u_R}{2} \right)^2} \right] \tag{65}$$

A.1.3   Solution of the Riemann problem

Using the above results, we can construct the exact solution of the Riemann problem (52). For the first characteristic field, we can construct a function $p_1(u, W_L)$ defined as:

$$p_1(u, W_L) = \begin{cases} p \text{ obtained from (64) for } u \leq u_L & (1 - \text{shock}), \\[2mm] p \text{ obtained from (58) for } u \geq u_L & (1 - \text{rarefaction}). \end{cases} \tag{66}$$

From general results on hyperbolic system (see e.g. [19, 26]), we know that $p_1(u, W_L)$ is a continuously differentiable function of u. In the same way, for the second characteristic field, we define a function $p_2(u, W_R)$ as follows:

$$p_2(u, W_R) = \begin{cases} p \text{ obtained from (60) for } u \leq u_R & (2 - \text{rarefaction}), \\[2mm] p \text{ obtained from (65) for } u \geq u_R & (2 - \text{shock}). \end{cases} \tag{67}$$

The states W_L and W_R being given, the intermediate state W^* between the two waves, as well as the nature of these two waves, is determined by solving the equation:

$$p_1(u^*, W_L) = p_2(u^*, W_R) \quad (= p^*) . \tag{68}$$

We can easily obtain a numerical evaluation of W^* using Newton's method for the solution of (68) (we know explicitly the first derivatives of p_1 and p_2). For example, if we choose $W_L = (1, 10)^T$ and $W_R = (-1, 20)^T$, we obtain a 1-shock and a 2-rarefaction with $W^* = (-2.9728, 11.6615)^T$; for this particular case, the curves p_1 and p_2 are shown on Figure 35.
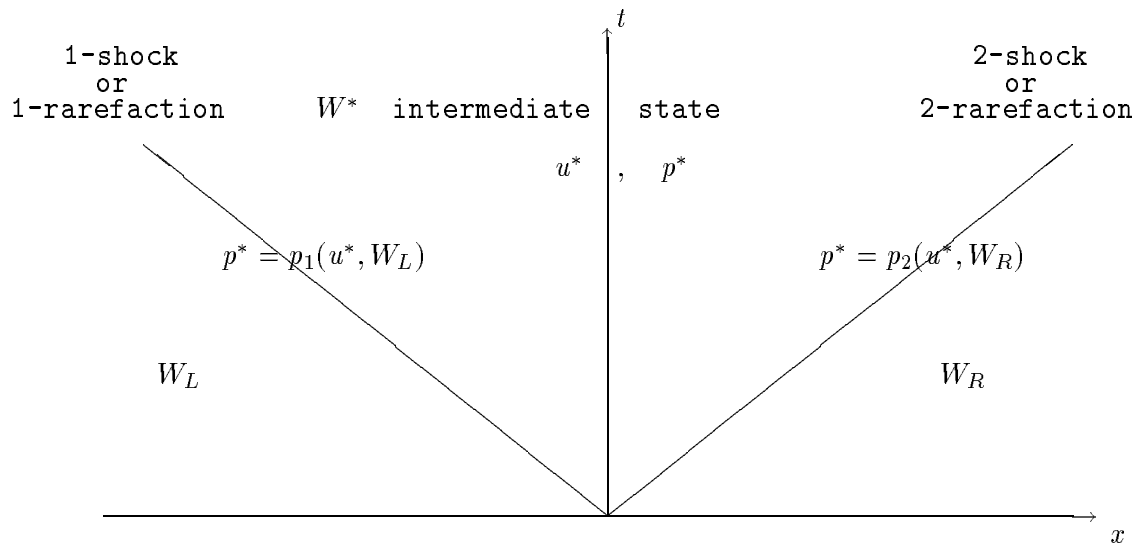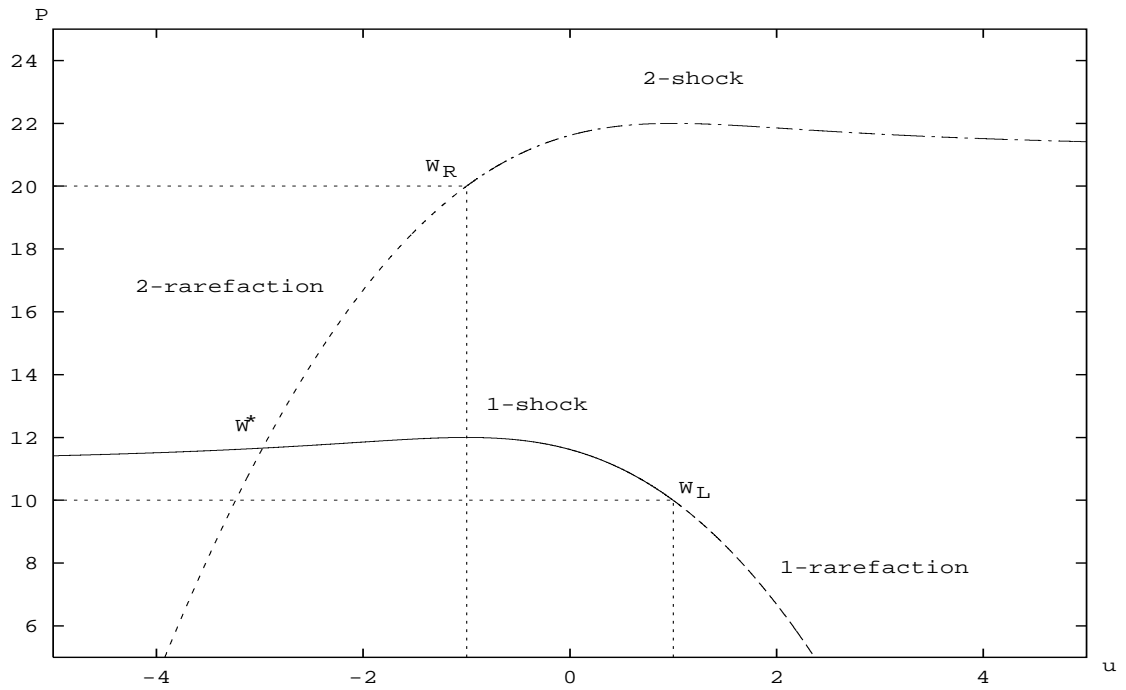
Figure 34 : The solution of Riemann problem

Figure 35 : The curves $p_1(u, W_L)$, $p_2(u, W_R)$ and the intermediate state W^*

Once W^* is determined, the exact solution of the Riemann problem is known. For instance, if the first wave is a 1-shock of speed s, we have (we are still denoting $\sigma = \dfrac{x}{t}$):

$$W(\sigma) = \begin{cases} W_L & \text{for } \sigma < s , \\[2mm] W^* & \text{for } \sigma > s , \end{cases} \tag{69}$$

whereas, in the case of a 1-rarefaction, we have:

$$W(\sigma) = \begin{cases} W_L & \text{for } \sigma \leq \lambda_1(W_L) , \\[3mm] (u(\sigma), p_1(u(\sigma), W_L))^T \text{ with } u(\sigma) = \dfrac{1}{2}\left(\sigma - \dfrac{k^2}{\sigma}\right) & \text{for } \lambda_1(W_L) \leq \sigma \leq \lambda_1(W^*) , \\[3mm] W^* & \text{for } \sigma \geq \lambda_1(W^*) . \end{cases} \tag{70}$$

Similar expressions hold for the second wave.

In the general case, it is easy to check the following facts:

- If $u_L \leq 0$, then $p_1(u, W_L)$ is a monotone decreasing function of u on $\mathbb{R}$;

- if $u_L > 0$, then $p_1(u, W_L)$ is a monotone increasing function of u on an interval $]-\infty, u_1]$ and monotone decreasing on the interval $[u_1, +\infty[$, with $u_1 < u_L$. Moreover, in both cases, it satisfies:

$$\lim_{u \to -\infty} p_1(u, W_L) = p_L + k^2 , \quad \lim_{u \to +\infty} p_1(u, W_L) = -\infty .$$

- If $u_R \geq 0$, then $p_2(u, W_R)$ is a monotone increasing function of u on $\mathbb{R}$;

- if $u_R < 0$, then $p_2(u, W_R)$ is a monotone increasing function of u on an interval $]-\infty, u_2]$ and monotone decreasing on the interval $[u_2, +\infty[$, with $u_2 < u_L$. Moreover, in both cases, it satisfies:

$$\lim_{u \to -\infty} p_2(u, W_R) = -\infty , \quad \lim_{u \to +\infty} p_2(u, W_R) = p_R + k^2 .$$

From these observations, it is easy to deduce that the curves $p_1(u, W_L)$ and $p_2(u, W_R)$ always intersect. Thus, we can determine, for any pair (W_L, W_R), an exact solution of the Riemann problem (52) consisting of two waves, the left wave being either a 1-rarefaction or an entropic 1-shock, the right wave being either a 2-rarefaction or an entropic 2-shock. Here, W_L and W_R no longer need to be close to each other.

We illustrate this result with three examples, where the possible different cases of waves appear. We set here $k = 1$.

- $W_L = (1, 10)$, $W_R = (-1, 20)$: the waves are a 1-shock and a 2-rarefaction (see Figure 35 and Figure 36);

- $W_L = (1, 10)$, $W_R = (-1, 10)$: the solution involves two shock waves (see Figure 37);

- $W_L = (-1, 5)$, $W_R = (1, 5)$: the three constant states are separated by two rarefaction waves (see Figure 38).

We compare these exact solutions with the numerical solutions on Figures 36, 37 and 38. The numerical solution is obtained with a first-order accurate explicit scheme with a CFL number of 0.65 and 101 mesh points. The numerical and analytic solutions are shown at time $t = 0.05$.

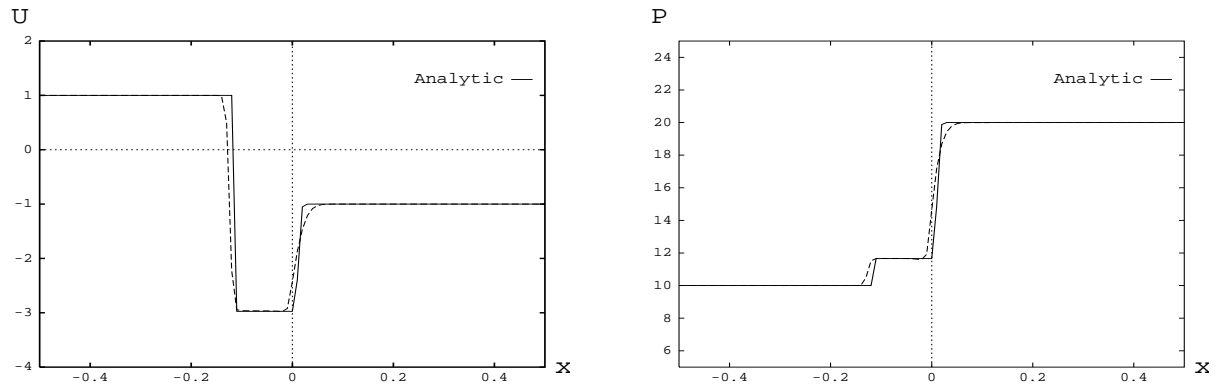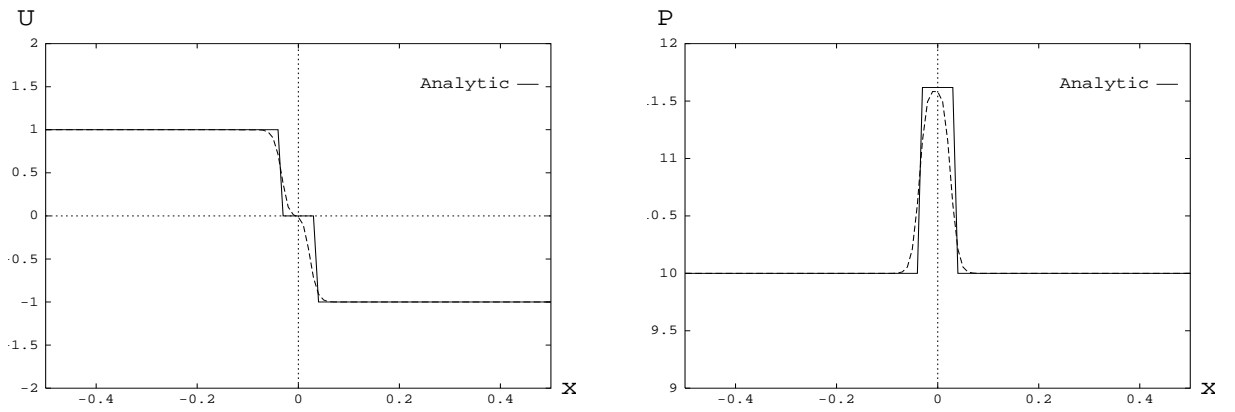Figure 36 : $W_L = (1, 10)$, $W_R = (-1, 20)$: Analytic and numerical solutions

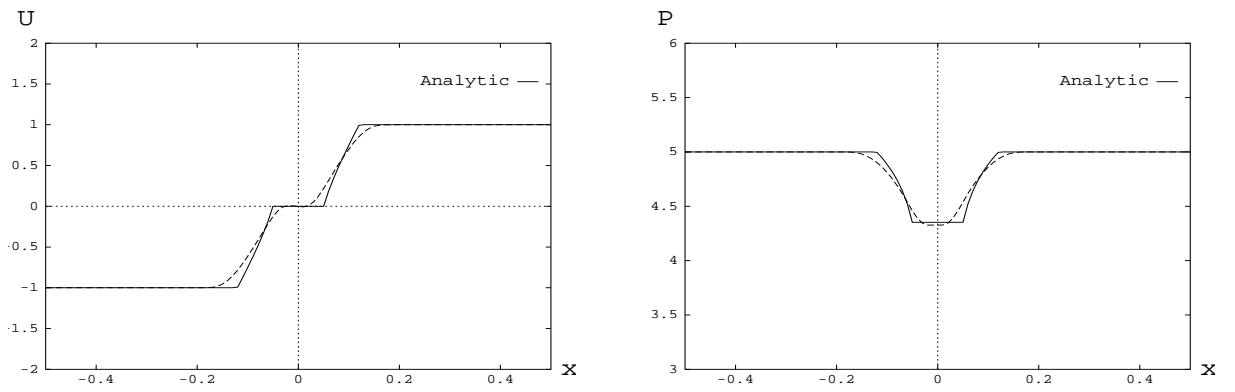Figure 37 : $W_L = (1, 10)$, $W_R = (-1, 10)$: Analytic and numerical solutions

Figure 38 : $W_L = (-1, 5)$, $W_R = (1, 5)$: Analytic and numerical solutions

A.1.4   Other upwind schemes

Beside the Roe scheme written in Section 3.1 above, the results of the previous sections allow us to construct two other upwind schemes for the solution of system (50).

First, it is clear that we can use our knowledge of the exact solution of the Riemann problem in order to construct a Godunov scheme for this system. Calling $V(\frac{x}{t}; W_L, W_R)$ the exact solution of the Riemann problem (52), then the Godunov numerical flux function can be expressed by:

$$\Phi^{God}(W_L, W_R) = F\left(V(0; W_L, W_R)\right) \ .$$

The only comment we add here is that, because of our remarks on the signs of both the eigenvalues of the Jacobian matrix A and the shock speeds s in the preceding sections, it is easy to check that the state $V(0; W_L, W_R)$ is always the intermediate constant state W^*.

Also, since we know the Riemann invariants for system (50), we can define an Osher numerical flux function:

$$\Phi^{Osher}(W_L, W_R) = \frac{F(W_L) + F(W_R)}{2} - \frac{1}{2}\int_{W_L}^{W_R} |A(W)|dW \ , \tag{71}$$

where the integration is made on a path connecting W_L to W_R in the state space. This path Γ consists of two subpaths Γ_1 and Γ_2 which are respectively parallel to the first and second eigenvectors r_1 and r_2. The state $\tilde{W}$ at the intersection of Γ_1 and Γ_2 satisfies:

$$\phi_1(\tilde{W}) = \phi_1(W_L) \ , \quad \phi_2(\tilde{W}) = \phi_2(W_R) \ .$$

From the definitions (57), (59) of the Riemann invariants ϕ_1 and ϕ_2, it is easy to see that $\tilde{W}$ can always be determined, for any pair (W_L, W_R).

Then, the evaluation of the integral in (71) is classical. For instance, we have:

$$\int_{W_L}^{\tilde{W}} |A(W)| \ dW = \int_{W_L}^{\tilde{W}} sign[\lambda_1(W)] \ A(W) \ dW \ .$$

Since $\lambda_1(W)$ is always negative we may write:

$$\int_{W_L}^{\tilde{W}} |A(W)| \ dW = F(W_L) - F(\tilde{W}) \ .$$

In the same way, using the positivity of λ_2, we have $\int_{\tilde{W}}^{W_R} |A(W)| \ dW = F(W_R) - F(\tilde{W})$, and we finally obtain:

$$\Phi^{Osher}(W_L, W_R) = F\left(\tilde{W}(W_L, W_R)\right) \ .$$

A.2   Two-dimensional flow with constant density

Let us come back to the following system:

$$\begin{cases} u_t + (u^2 + p)_x + (uv)_y = 0 \ , \\[2mm] v_t + (uv)_x + (v^2 + p)_y = 0 \ , \\[2mm] p_t + k^2(u_x + v_y) \ = \ 0 \ , \end{cases} \tag{72}$$

which arises in the framework of the artificial compressibility approximation for a two-dimensional flow. More precisely, we will see how the preceding results about the one-dimensional system (50) can be useful for the two-dimensional system (72).

We will again denote here:

$$W = \begin{pmatrix} u \\ v \\ p \end{pmatrix} \ , \quad F(W) = \begin{pmatrix} u^2 + p \\ uv \\ k^2 u \end{pmatrix} \ , \quad G(W) = \begin{pmatrix} uv \\ v^2 + p \\ k^2 v \end{pmatrix} \ . \tag{73}$$

We already commented the fact that system (72) is not physically correct. But it is easy to see that this system retains the rotational invariance of the original "incompressible" equations. This is the key observation for designing a finite volume approximation of (72) (see e.g. [19]). Indeed, thanks the rotational invariance, evaluating the flux $\displaystyle\int_{\partial C_i \cup \partial C_j} Fn_x + Gn_y$ between two neighbor finite volumes C_i and C_j amounts to solving the one-dimensional Riemann problem:

$$\begin{cases} W_t + F(W)_x = 0 \ \ \text{for } x \in \mathbb{R} \ , \ \ t \geq 0 \ , \\[2mm] W(x,0) = \begin{cases} W_L & \text{if } x < 0 \ , \\ W_R & \text{if } x > 0 \ , \end{cases} \end{cases} \tag{74}$$

but now with the definitions (73) of W and F.

Of course, there is a close relation between this Riemann problem and the simpler one (52). Since the variable v does not influence two of the three equations in (74), it is easy to see that the solution of (74) can be deduced from the solution of (52). More precisely, for any pair (W_L, W_R), this solution can be constructed in two steps:

- Using the values of (u_L, p_L) and (u_R, p_R), construct the solution $(u(\sigma), p(\sigma))$ of the 2×2 Riemann problem (52) (with $\sigma = \dfrac{x}{t}$); call $W^* = (u^*, p^*)^T$ the intermediate state between the two waves;

- Complete the solution of (74) by setting:

$$v(\sigma) = \begin{cases} v_L & \text{for } \sigma < u^* \ , \\[2mm] v_R & \text{for } \sigma > u^* \ . \end{cases} \tag{75}$$

In particular, we can easily define a Godunov and an Osher scheme for system (72).

2.A.3 One-dimensional flow with non constant density

Lastly, let us examine the system:

$$
\begin{cases}
\rho_t + (\rho u)_x = 0 \ , \\[2mm]
(\rho u)_t + (\rho u^2 + p)_x = 0 \ , \\[2mm]
p_t + k^2 u_x = 0 \ ,
\end{cases}
\tag{76}
$$

taken from system (46) with a variable density, but in a one-dimensional geometry.

Although we again have here a 3×3 system, the analysis below will show surprising differences with the previous problem (72).

Let us now set:

$$
W = \begin{pmatrix} \rho \\ \rho u \\ p \end{pmatrix} \ , \quad
F(W) = \begin{pmatrix} \rho u \\ \rho u^2 + p \\ k^2 u \end{pmatrix} \ .
\tag{77}
$$

The Jacobian matrix:

$$
A(W) = \frac{\partial F}{\partial W} = \begin{pmatrix}
0 & 1 & 0 \\[2mm]
-u^2 & 2u & 1 \\[2mm]
-\dfrac{k^2}{\rho} u & \dfrac{k^2}{\rho} & 0
\end{pmatrix}
\tag{78}
$$

has three real eigenvalues (assuming $\rho > 0$):

$$
\lambda_1 = \frac{u}{2} - \sqrt{(\frac{u}{2})^2 + \frac{k^2}{\rho}} \ , \quad
\lambda_2 = u \ , \quad
\lambda_3 = \frac{u}{2} + \sqrt{(\frac{u}{2})^2 + \frac{k^2}{\rho}} \ .
$$

associated respectively with the three following right eigenvectors:

$$
r_1 = \begin{pmatrix} 1 \\ \lambda_1 \\ \lambda_3^2 \end{pmatrix} \ , \quad
r_2 = \begin{pmatrix} 1 \\ u \\ 0 \end{pmatrix} \ , \quad
r_3 = \begin{pmatrix} 1 \\ \lambda_3 \\ \lambda_1^2 \end{pmatrix} \ .
$$

Thus, the system is strictly hyperbolic. Moreover, a straightforward calculation, which we omit here, shows that *all three characteristic field are linearly degenerate*, i.e. that:

$$
\nabla \lambda_i . r_i = 0 \ ,
$$

for $i = 1$, 2 or 3. Therefore, at least when the states W_L and W_R are close enough to each other, there exists a solution to the Riemann problem for system (76), which consists of four constant states W_L, W_2, W_3 and W_R, separated by three contact discontinuities (a rather unusual situation).

A.2.1   Contact discontinuities

Let us investigate more precisely these discontinuities. This will be done by using both the Riemann invariants and the Rankine-Hugoniot relations.

We begin with the first characteristic field. A function $\phi(W)$ is a 1-Riemann invariant if it satisfies the following relation (we set $m = \rho u$):

$$\frac{\partial \phi}{\partial \rho} + \lambda_1 \frac{\partial \phi}{\partial m} + \lambda_3^2 \frac{\partial \phi}{\partial p} = 0 \ .$$

We already know that λ_1 is a 1-Riemann invariant. Moreover, it is easy to check that $p + \dfrac{k^4}{\rho \lambda_1^2}$ is also a 1-Riemann invariant.

From these observations, we deduce that:

$$p_2 = p_L + \frac{k^4}{\rho_L \lambda_1 (W_L)^2} - \frac{k^4}{\rho_2 \lambda_1 (W_L)^2} \ . \tag{79}$$

Since we also have $k^2(u_2 - u_L) = \lambda_1(W_L)(p_2 - p_L)$ from the Rankine-Hugoniot relations, we get:

$$u_2 = u_L + \frac{\lambda_1(W_L)}{k^2}(p_2 - p_L) \ , \tag{80}$$

which together with (79), yields:

$$u_2 = u_L + \frac{k^2}{\lambda_1(W_L)} \left(\frac{1}{\rho_L} - \frac{1}{\rho_2} \right) \ . \tag{81}$$

Similar results hold for the third contact discontinuity. We get here the two relations:

$$u_3 = u_R + \frac{\lambda_3(W_R)}{k^2}(p_3 - p_R) \ , \tag{82}$$

$$u_3 = u_R + \frac{k^2}{\lambda_3(W_R)} \left(\frac{1}{\rho_R} - \frac{1}{\rho_3} \right) \ . \tag{83}$$

Lastly, the case of the second contact discontinuity is even simpler. Indeed, since p clearly appears to be a 2-Riemann invariant, we have:

$$u_2 = u_3 \ , \quad p_2 = p_3 \ . \tag{84}$$

A.2.2   The solution of the Riemann problem

Using (80), (82) and (84), the pressure and the velocity of the two intermediate states can be expressed in terms of W_L and W_R. Denoting now $u_2 = u_3 = u^*$, $p_2 = p_3 = p^*$, we have:

$$p^* = \frac{k^2(u_L - u_R) + p_R\lambda_3(W_R) - p_L\lambda_1(W_L)}{\lambda_3(W_R) - \lambda_1(W_L)} \ ,$$

(85)

$$u^* = \frac{k^2(\lambda_3(W_R)u_L - \lambda_1(W_L)u_R) + \lambda_1(W_L)\lambda_3(W_R)(p_R - p_L)}{k^2(\lambda_3(W_R) - \lambda_1(W_L))} \ .$$

Finally the density values are obtained from (81) , (83):

$$\rho_2 = \left[\frac{1}{\rho_L} - \frac{\lambda_1(W_L)^2 k^2(u_L - u_R) + \lambda_1(W_L)^2\lambda_3(W_R)(p_R - p_L)}{k^4(\lambda_3(W_R) - \lambda_1(W_L))}\right]^{-1} \ ,$$

$$\rho_3 = \left[\frac{1}{\rho_R} - \frac{\lambda_3(W_R)^2 k^2(u_L - u_R) + \lambda_1(W_L)\lambda_3(W_R)^2(p_R - p_L)}{k^4(\lambda_3(W_R) - \lambda_1(W_L))}\right]^{-1} \ .$$

The Riemann problem has an admissible solution if and only if $\rho_2 > 0$ and $\rho_3 > 0$, which means that some conditions on W_L and W_R have to be satisfied. In such a case, the solution is defined by:

$$W(\sigma) = \begin{cases} W_L & \text{for} \quad \sigma < \lambda_1(\mathrm{W_L}) \ , \\[2mm] W_2 = \begin{pmatrix} \rho_2 \\ \rho_2 u^* \\ P^* \end{pmatrix} & \text{for} \quad \lambda_1(\mathrm{W_L}) < \sigma < \mathrm{u}^* \ , \\[2mm] W_3 = \begin{pmatrix} \rho_3 \\ \rho_3 u^* \\ P^* \end{pmatrix} & \text{for} \quad \mathrm{u}^* < \sigma < \lambda_3(\mathrm{W_R}) \ , \\[2mm] W_R & \text{for} \quad \lambda_3(\mathrm{W_R}) < \sigma \ . \end{cases}$$

(86)

This result allows us to construct a Godunov scheme for system (76) (for this system, the Osher scheme exactly reduces to the Godunov scheme). Also, as in section 2.A.2 above, these results can be extended to the two-dimensional system (46) using the rotational invariance.
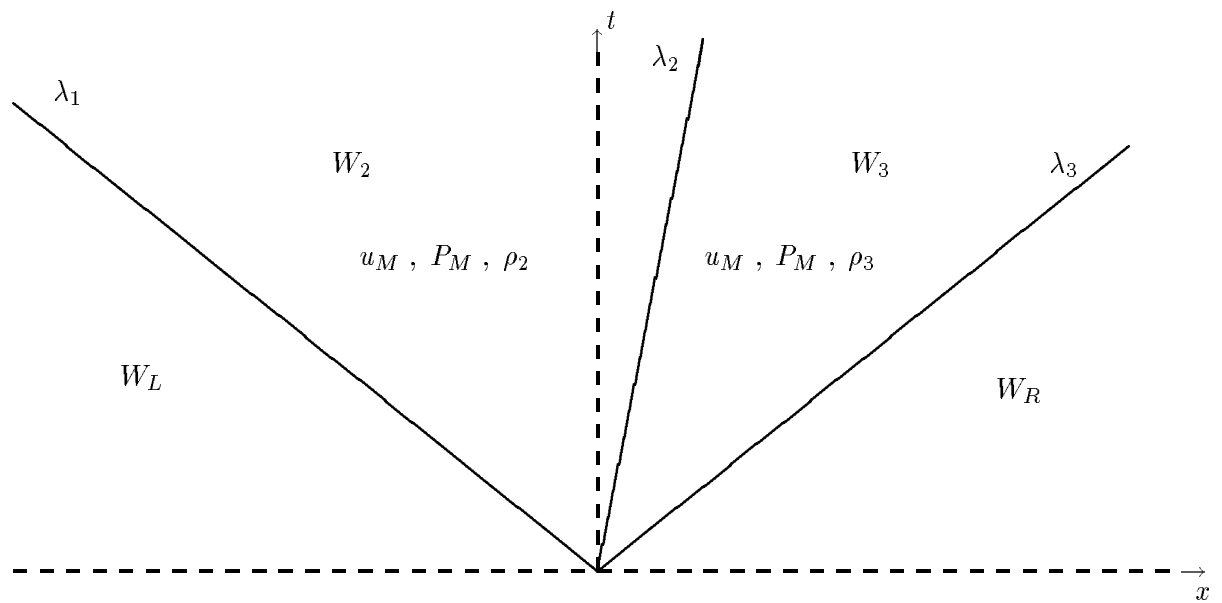
Figure 39 : The Riemann problem solution

B   Appendix 2: Stability analysis in 1-D

We are interested in the solution of the convection equation $u_t + c\, u_x = 0$ where $c > 0$.

Using the following spatial discretization of $]0, 1[$:

$$\Delta x = \frac{1}{N} \quad, \quad x_j = j\Delta x \ \text{ for } \ j = 0, \cdots, N$$

we get the semi–discretized system of equations :

$$\frac{d}{dt} u_j(t) = \Psi_j(u(t)) \quad \text{for } \ j = 1, \cdots, N-1$$

where $u_j(t) = u(x_j, t)$ and where $\Psi_j(u(t))$ is an approximation of $-c[u(x_{j+\frac{1}{2}}, t) - u(x_{j-\frac{1}{2}}, t)]$.

Using Von Neumann analysis method, we insert a harmonic data

$$\tilde{u}_j^n = \tilde{u}_k\, e^{ij\theta_k} \quad \text{with } \ \theta_k = \frac{k\pi}{N} \quad k = 0, \cdots, \pm N$$

and we obtain :

$$\frac{d\tilde{u}_k}{dt} = \lambda_{\theta_k} \tilde{u}_k^n \ .$$

More precisely we give for four particular spatial schemes the expression of $\Psi_j(u)$ followed by the expression of λ_θ.

The three-points centered scheme , which is second-order accurate in space:

$$(S_1) \qquad \begin{cases} \Psi_j(u) = -\dfrac{c}{2\Delta x}(u_{j+1} - u_{j-1}) \\[4mm] \lambda_\theta = -\dfrac{c}{\Delta x} i \sin\theta \end{cases}$$

The totaly upwind first-order scheme :

$$(S_2) \qquad \begin{cases} \Psi_j(u) = -\dfrac{c}{\Delta x}(u_j - u_{j-1}) \\[4mm] \lambda_\theta = -\dfrac{c}{\Delta x}\{(1 - \cos\theta) + i\sin\theta\} \end{cases}$$

The partly-upwind second-order scheme , which we obtain when $\delta = 1$ in (7); we can notice that for $\beta = 0$ we get the scheme (S_1) above, and that we obtain a third-order accurate scheme when $\beta = \dfrac{1}{3}$:

$$(S_3) \quad \begin{cases} \Psi_j(u) = -\dfrac{c}{2\Delta x}(\beta u_{j-2} - (1 + 3\beta)u_{j-1} + 3\beta u_j + (1 - 3\beta)u_{j+1}) \\[3mm] \lambda_\theta = -\dfrac{c}{2\Delta x}\{3\beta - 4\beta\cos\theta + \beta\cos 2\theta) + i(2(1+\beta)\sin\theta - \beta sin2\theta)\} \end{cases}$$

The five-points second-order accurate centered scheme which we obtain when $\delta = 1$ in (7); as previously, we get the three-points centered scheme (S_1) when β is equal to zero, and we get a fourth-order accurate scheme when $\beta = \dfrac{1}{3}$.

$$(S_4) \quad \begin{cases} \Psi_j(u) = -\dfrac{c}{4\Delta x}(\beta u_{j-2} - 2(\beta+1)u_{j-1} + 2(\beta+1)u_{j+1} - \beta u_{j+2}) \\[3mm] \lambda_\theta = -\dfrac{c}{4\Delta x}i\{4(1+\beta)\sin\theta - \beta\sin 2\theta)\} \end{cases}$$

For the time discretization we use a Runge-Kutta fourth-order accurate method in which we obtain $u^{n+1} = u_j(t^{n+1})$ starting from $u^n = u_j(t^n)$ in the following way:

$$\begin{cases} u^{(0)} = u^n \\[3mm] u^{(k)} = u^{(0)} + \alpha_k\,\Delta t\,\Psi(u^{(k-1)})\ \ k = 1,\cdots,4 \\[3mm] u^{n+1} = u^{(4)} \end{cases}$$

The coefficients α_k have to verify :

- $0 < \alpha_k \leq 1$,

- $\alpha_4 = 1$ to obtain the consistence of the scheme,

- $\alpha_3 = \dfrac{1}{2}$ if we choose to have a second-order time accuracy.

The stability domain of this method can be written as :

$$\mathcal{D} = \{\, z \,\epsilon\, \mathbb{C} \ /\ |g(z)| < 1\,\}$$

where the amplificator factor $g(z)$ can be expressed as :

$$g(z) = 1 + z + \frac{1}{2}(z^2 + \alpha_2 z^3 + \alpha_2\,\alpha_1 z^4)\ .$$

So $\mathcal{D}$ depends only of the two coefficients α_1 and α_2.

For each particular spatial approximation, we can determine the maximal Courant number

$$\sigma_{max} = \left(c\,\frac{\Delta t}{\Delta x} \right)_{max}$$

which ensures the stability, i.e. such that $\lambda_\theta\,\Delta t$ is in the stability domain $\mathcal{D}_{(\alpha_1,\alpha_2)}$ for all θ in $[-\pi,\pi]$.

We now search a couple of coefficients (α_1,α_2) that give the biggest possible σ_{max}.

For the scheme (S_3), we obtain the following coefficients:

- for $\beta = \dfrac{1}{6}$: $\alpha_1 = 0.199$ $\alpha_2 = 0.312$ and $\sigma_{max} = 2.62$,

- for $\beta = \dfrac{1}{3}$: $\alpha_1 = 0.166$ $\alpha_2 = 0.307$ and $\sigma_{max} = 2.20$.

Their stability domains are represented respectively on Figure 40 and 41.

For the five-points centered scheme (S_4) with $\beta = \dfrac{1}{3}$ we obtain the following values (see $\mathcal{D}_{(\alpha_1,\alpha_2)}$ on Figure 43) :

- $\alpha_1 = \dfrac{1}{4}$ $\alpha_2 = \dfrac{1}{3}$ and $\sigma_{max} = 2.06$.

Lastly, for the upwind first-order scheme (S_2) we find :

- $\alpha_1 = 0.14$ $\alpha_2 = 0.32$ and $\sigma_{max} = 2.14$.

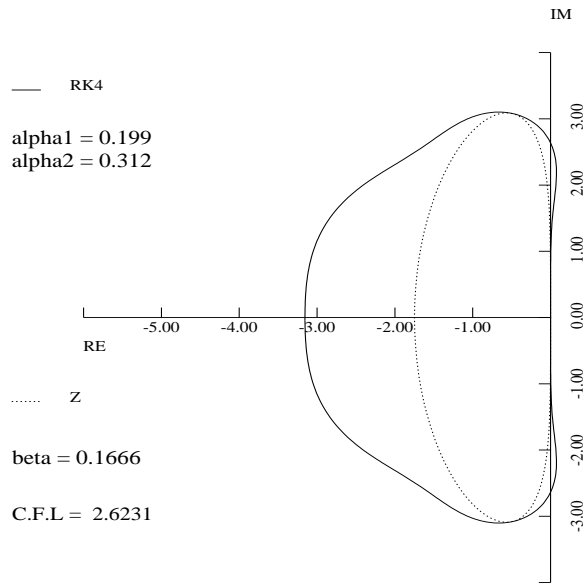The stability domain is given on Figure 42 .

_____ RK4

alpha1 = 0.199
alpha2 = 0.312

.... Z

beta = 0.1666

C.F.L = 2.6231

Figure 40 : Stability domain: (S_3) $\beta = \dfrac{1}{6}$

_____ RK4

alpha1 = 0.166
alpha2 = 0.307
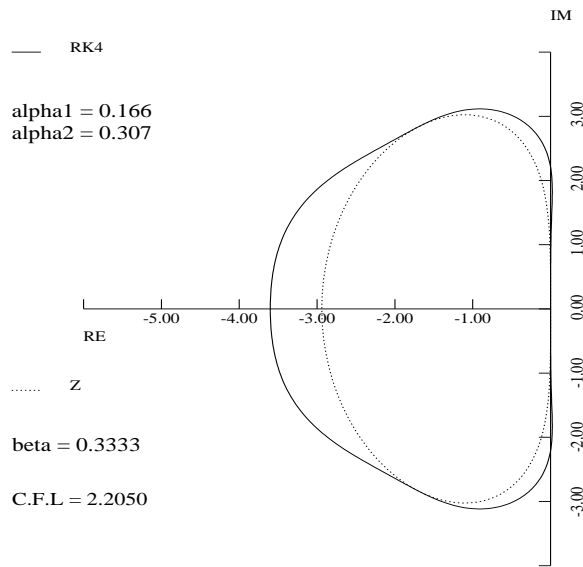
...... Z

beta = 0.3333

C.F.L = 2.2050

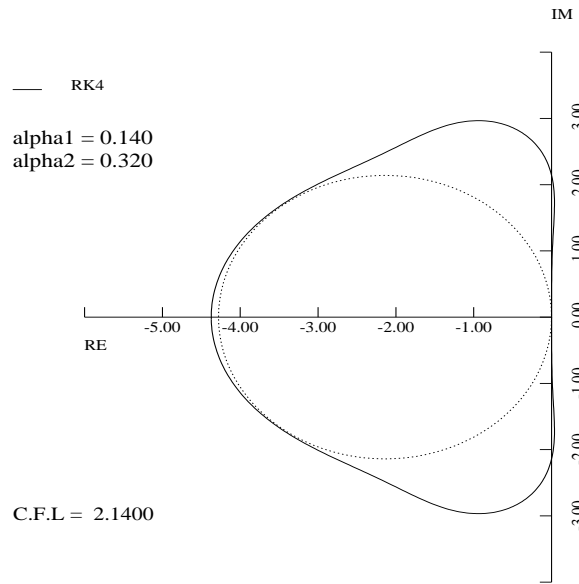Figure 41 : Stability domain (S_3) $\beta = \dfrac{1}{3}$

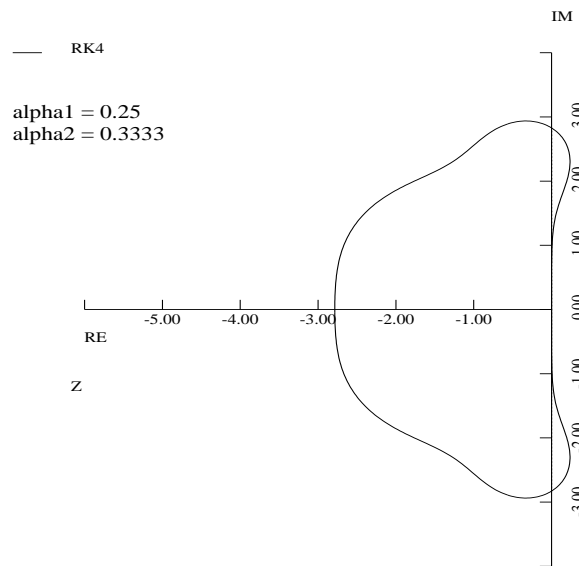Figure 42 : Stability domain : upwind first-order accuracy

Figure 43 : Stability domain : classical RK4

REFERENCES

[1] M. BUFFAT *"Etude de la simulation numérique par une méthode d'éléments finis des écoulements internes subsoniques instationnaires bi et tridimensionnels"*, Thèse de doctorat d'état ès sciences, Université Claude Bernard (Lyon I) (1991).

[2] O.R. BURGGRAF, *"Analytical and Numerical Studies of the Structure of Steady Separated Flow"*, J. of Comp. Phys., **24**, p. 113-151 (1966).

[3] J.A. DESIDERI, A. GOUDJO, V. SELMIN, *"Third-Order Numerical Schemes for Hyperbolic Problems"*, Rapport de Recherche INRIA N° 607 (1987).

[4] J.A. DESIDERI, P.W. HEMKER, *"Analysis of the convergence of iterative implicit and defect-correction algorithms for hyperbolic problems"*, Rapport de Recherche INRIA N° 1200 (1990).

[5] A. DERVIEUX, L. FEZOUI, F. LORIOT, *"On High Resolution Extensions of Lagrange-Galerkin Finite-Element Schemes"*, Rapport de Recherche INRIA N°1703 (1992).

[6] E. DICK, *"A Multigrid Method for Steady Incompressible Navier-Stokes Equations Based on Partial Flux Splitting"*, Int. J. Num. Meth. Fluids, **9**, p. 113-120 (1989).

[7] C. FARHAT, L. FEZOUI, S. LANTERI, *"Two-Dimensional Viscous Flow Computations on the CM-2: Unstructured Meshes, Upwind Schemes and Massively Parallel Computations"*, Technical Report, University of Colorado at Boulder, No. CU-CSSC-91-26 (1991).

[8] G. FERNANDEZ, H. GUILLARD, *"A Numerical Method for the Computation of Low Mach Number Reactive Flows"*, Proc. 6th Int. Conf. Numerical methods in laminar and turbulent flows (Eds C. Taylor, P. Gresho, R.L. Sani & J. Häuser), Swansea (1989).

[9] L. FEZOUI, S. LANTERI, B. LARROUTUROU, C. OLIVIER, *"Résolution numérique des équations de Navier-Stokes pour un fluide compressible en maillage triangulaire"*, Rapport de Recherche INRIA N° 1033 (1989).

[10] M. FORTIN, R. PEYRET, R. TEMAM, *"Résolution numérique des équations de Navier-Stokes pour un fluide incompressible"*, Journal de Mécanique, **10**, N°3 (1971).

[11] M. FORTIN, F. THOMASSET, *"Mixed Finite-Element Methods for Incompressible Flow Problems"*, J. of Comp. Phys., **31**, p. 113-145 (1979).

[12] D. GREENSPAN, Comput. J., **12**, p. 89-96 (1969).

[13]   U. GHIA, K.N. GHIA, C.T. SHIN, *"High-Re Solutions for Incompressible Flow Using the Navier-Stokes Equations and a Multigrid Method"*, J. of Comp. Phys., **48**, p. 387-411 (1982).

[14]   V. GIRAULT, P.A. RAVIART, *"Finite Element Methods for Viscous Incompressible Flows"*, Springer-Verlag, Berlin (1986).

[15]   A. HARTEN, P.D. LAX, B. VAN LEER, *"On upstream differencing and Godunov-type schemes for hyperbolic conservation laws"*, Society for Industrial and Applied Mathematics, **25**, $N°1$ (1983).

[16]   T.R.J. HUGHES, A.N. BROOKS, *"A multidimensional upwind scheme with no crosswind diffusion"*, in Finite Element methods for Convection Dominated Flows, (Hughes, T.H.R. ed.), AMD, **34**, p. 19-35, ASME New York (1979).

[17]   N. KONDO, N. TOSAKA, T. NISHIMURA, *"High Reynolds solutions of the Navier-Stokes equations using the third-order finite element method"*, Proceedings of Computational Methods in Flow Analysis, 984-991, Eds. Niki H. and Kawahara M., Okayama Univ. of Science (1988).

[18]   M.H. LALLEMAND, *"Dissipative properties of Runge-Kutta Schemes with Upwind Spatial Approximation for the Euler Equations"*, Rapport de Recherche INRIA $N°$ 1173 (1990).

[19]   P. D. LAX, *"Hyperbolic systems of convervation laws and the mathematical theory of shock waves"*, CBMS regional conference series in applied mathematics, **11**, SIAM, Philadelphia (1972).

[20]   M. NALLASAMY, K.K. PRASAD, *"On cavity flow at high Reynolds numbers"*, J. Fluid Mech., **79**, p. 391-414 (1977).

[21]   R. PIERRE, *"Regularization procedures of mixed finite element approximations of the Stokes problem"* Rapport de Recherche INRIA $N°673$ (1987).

[22]   PULLIAM T.H., *"Low Reynolds Number Numerical Solutions of Chaotic Flows"*, AIAA Paper $N°$ 89-0123 (1989).

[23]   C.M. RHIE, W.L. CHOW, *"Numerical Study of the Turbulent Flow past an Airfoil with Trailing Edge Separation"*, AIAA J., **21**, p. 1525-1532 (1983).

[24]   P. L. ROE, *"Approximate Riemann Solvers, Parameters Vectors and Difference Schemes"*, J. of Comp. Phys., **43**, p. 357-371 (1981).

[25]   Ph. ROSTAND, B. STOUFFLET, *Finite Volume Galerkin Methods for Viscous Gas Dynamics*, Rapport de Recherche INRIA $N°$ 863 (1988).

[26]   J. SMOLLER, *"Shock waves and reaction-diffusion equations"*, Springer Verlag, New-York (1983).

[27] J. STEGER, R.F. WARMING, *"Flux vector splitting for the inviscid gas dynamic with applications to finite-difference methods"*, J. of Comp. Phys., **40**, (2), p. 263-293, (1981).

[28] M. TABATA, S. FUJIMA, *"A finite element scheme for the Navier-Stokes equations using a third-order upwind approximation"*, Finite Element in Flow problems, Hunstville (1988).

[29] F. THOMASSET, *"Implementation of Finite Element Methods for Navier-Stokes Equations "*, Springer series in computational physics (1981).

[30] S. TUANN, M. OLSON, *"Studies of rectangular cavity flow with Reynolds number by a finite element method"*, Structural Research Series Report N° 19, I.S.S.N. 0318-3378, Vancouver British Columbia (1977).

[31] B. VAN LEER, *"Towards the Ultimate Conservative Difference Scheme V : a Second-Order Sequel to Godunov's Method"*, J. of Comp. Phys., **32** (1979).

[32] R.F. WARMING, B.J. HYETT, *"The modified Equation Approach to the Stability and Accuracy Analysis of Finite-Difference Methods"*, J. of Comp. Phys., **14**, p. 159-179 (1975).

[33] J.E. WELCH, F.H. HARLOW, J.P. SHANNON. B.J. DALY, *"The MAC Method, a computing technique for solving viscous incompressible transient fluid flow Problem involving free surfaces"*, LA-3425, Los Alamos, New-Mexico (1966).